Tuneable Hybrid and Multimode Squeezed States of Light

by

Christian Drago

A thesis
presented to the University of Waterloo
in fulfillment of the
thesis requirement for the degree of
Masters of Science
in
Physics

Waterloo, Ontario, Canada, 2020

Author's Declaration

I hereby declare that I am the sole author of this thesis. This is a true copy of the thesis, including any required final revisions, as accepted by my examiners.

I understand that my thesis may be made electronically available to the public.

Abstract

Gaussian quantum states of light have many applications in quantum technologies. Two of the most widely used Gaussian quantum states of light are the single- and two-mode squeezed states. In this thesis, we propose the generation of a hybrid of these two states, which has both properties of single- and two-mode squeezed states. We then extend our method to the generation of multimode squeezed states which posses N-partite entanglement.

Our states are defined using Gaussian frequency modes, and our method relies on a nonlinear-optical process called spontaneous parametric downconversion. We shape the joint spectral amplitude of the generated light in two ways, by spectrally engineering the light incident on the crystal and by the engineering of the nonlinear crystal to have desired properties. We first use our method to generate tuneable hybrid squeezed states and then extend it to multimode squeezed states. We then investigate design considerations for the nonlinear crystal and study the effect of fabrication errors.

The tuneable hybrid and multimode squeezed states are localized in both frequency and time, making them ideal for a variety of quantum information protocols. We expect that the states will be used to generalize many quantum information protocols to their multi-mode counterparts, such as, multi-parameter quantum metrology, multi-channel quantum imaging and multi-partite teleportation. Our work will therefore broaden the applicability of optics for the development of quantum technologies.

Acknowledgements

First and foremost, I want to thank Agata M Brańczyk, for being both a supervisor and friend. Thank you for always being there whenever I had a question or needed advice. Your guidance helped me to become a better scientist. I am grateful for all that you provided during my M.Sc. degree, especially through the final days of preparing this thesis.

Thank you to Christine Muschik and Robert Mann for being a part of my advising committee, and to Michal Bajcsy for reviewing this thesis and attending my defence.

I would like to thank my girlfriend Francesca and her parents, who have always treated me as one of their own.

Finally, I would like to thank both my parents for all that they have done. They have always allowed me the freedom to choose my own path and have supported me every step of the way.

Dedication

Dedicated to Francesca, who has stuck by me through everything.

Table of Contents

List of Figures ix

1 Introduction 1

2 Theory 4

2.1 Quantization of Light in a Linear Material 4

2.1.1 Classical Optics 4

2.1.2 Quantizing the Classical Electromagnetic Field 5

2.1.3 Quantum States of Light 6

2.2 Linear Optics 7

2.2.1 Polarizing Beam Splitter 7

2.2.2 Half-Wave Plate 8

2.2.3 Beam Splitter 8

2.3 Nonlinear Optics 9

2.3.1 Spontaneous Parametric Down conversion 9

2.3.2 The Downconverted State 11

2.3.3 The Pump Function 12

2.3.4 The Phasematching Function 12

2.3.5 The Joint Spectral Amplitude 12

2.4 Properties of the Phasematching Function 15

2.4.1 Uniform Crystal . . . 16
2.4.2 Group Velocity Matching . . . 16
2.4.3 Quasi Phasematching . . . 17
2.4.4 Ferroelectric Poling . . . 18
2.4.5 Motivating a Tailored Phasematching Function . . . 19
2.5 Nonlinearity Engineering . . . 20
2.5.1 Amplitude of a Uniform Crystal . . . 20
2.5.2 Algorithm for Tailoring a Nonlinear Crystal . . . 21

3 Encoding Modes as Gaussian Frequency Distributions 26
3.1 Single-Mode Squeezed Vacuum States . . . 27
3.2 Two-Single Mode Squeezed Vacuum States . . . 28
3.3 Two-Mode Squeezed Vacuum States . . . 30
3.4 Generalized Modes and Linear-Optical Transformations . . . 30
3.4.1 Extending Gaussian Frequency Distributions to Many Modes . . . 31
3.4.2 Linear-Optical Transformations . . . 31

4 Tunable Hybrid Squeezed States of Light 34
4.1 Pump Pulse Shaping . . . 36
4.2 Engineering the Phasematching Function . . . 38
4.3 The Joint Spectral Amplitude . . . 39
4.4 Providing a Decomposition of the Joint Spectral Amplitude . . . 41
4.5 Eliminating the Polarization Degree of Freedom . . . 42

5 Multimode Squeezed Vacuum States 45
5.1 Generalizing the Joint Spectral Amplitude . . . 46
5.2 Decomposing the Multimode Joint Spectral Amplitude . . . 46
5.3 Eliminating the Polarization Degree of Freedom for the Multimode State . . . 48
5.4 Generating the Joint Spectral Amplitude for Multimode Squeezed States . . . 49

6 Design Considerations and Fabrication Errors **52**

6.1 Constraints on the Target Phasematching Function 52

6.1.1 Shape of Target Phasematching function 52

6.1.2 Constraints on the Amplitude coefficients of the Target Phasematching Function 53

6.1.3 Optimal Width of the Target Phasematching Function 54

6.1.4 Sources of Error due to Oscillations of the Target Amplitude 55

6.1.5 Varying the Number of Domains 56

6.2 Fabrication Errors 58

7 Conclusion **63**

References **66**

APPENDICES **72**

A Phase Matching Function Constraints **73**

B Example of Custom Phase Matching Function **75**

B.1 Gaussian PMF 75

List of Figures

2.1 Schematic of a Type 2 SPDC process in a 1D wave guide. The pump photon is downconverted into two orthogonally polarized photons denoted signal and idler. The pump and signal photon is horizontally polarized and the idler is vertically polarized. The process is mediated by a crystal with a $\chi_{(2)}$ nonlinearity and is energy and momentum conserving. 10

2.2 Schematic drawing of a JSA for a typical SPDC process. 13

2.3 Typical pump,PMF and JSA for a SPDC process. 14

2.4 PMF for a uniform nonlinear crystal with different group velocities. 18

2.5 Showing how the nonlinearity in flipped by applied a field at a localized electrode. Figure was taken from [1]. 19

2.6 Crystal that has been ferroelectrically poled. The different shades of grey correspond to a nonlinearity that is either $+1$ or -1. This figure was taken from [2] with permission. 19

2.7 Schematic of nonlinear crystal used for calculating the nonlinearity in the algorithm. The crystal extends from $-L/2$ to $L/2$ and is centered at $z = 0$. The crystal is broken up into N pieces each with length l_c such that $L = Nl_c$ and indexed by m. In each domain the nonlinearity is either ± 1, in the above image the nonlinearity for the first three domains is +1,-1. In a real crystal N is typically on the order of $500 - 2000$. 23

3.1 Schematic JSA 28

3.2 Schematic JSA for a state corresponding to two SMSV states. The different colors represent different amplitudes. 29

3.3 Schematic JSA for a state corresponding to a TMSV state. 31

4.1 Schematic of the JSA corresponding to a state that is both single- and two-mode squeezed. Circles with different shading indicate different peak amplitudes. 35

4.2 Schematic of the JSA that would be produced by multiply a PUMP and PMF each with three Gaussian peaks. 36

4.3 Schematic for creating a pump pulse of light that has a frequency distribution of three gaussians. In the figure the colors red, green, blue represent the narrow frequency pulsed light. By removing the block we can change on the fly the input pump light. In the figure BS and M represent a beam splitter and mirror. 37

4.4 Pump frequency distribution for three Gaussian's at the same width and separation as the PMF in Fig. 4.6 plotted as a function of ω_p and ω_s, ω_i. The amplitudes coefficients for each peak are $b_{-1} = 4, b_0 = 3, b_1 = 6$. 37

4.5 Nonlinearity profile for a crystal with the target PMF given by Eq. (4.4). . 38

4.6 PMF as a function of Δk and the signal and idler frequencies for a target PMF given by Eq. (4.4). 39

4.7 JSA, PMF and pump. 40

4.8 JSA after filtering the horizontal and vertical frequency generation 41

4.9 Set of transformation to eliminate the polarization degree of freedom. The line style represents the polarization of light. P_1 and P_2 represent the spatial degrees of freedom, PBS is a polarizing beam splitter, HWP is a half wave plate, BS is a beam beam splitter and M is a mirror. Dashed and solid lines represent H and V polarization respectively. 43

5.1 Schmatic JSA for a PMF and PUMP made up of $2N + 1$ Gaussian. Each amplitude is centered at the frequency $\Omega_{-2N}, .., \Omega_0, ..., \Omega_{2N}$. For simplicity we keep the colour of each amplitude the same. 47

5.2 multimode JSA 50

6.1 Plotting the target amplitude for a Gaussian target PMF for different widths. 54

6.2 Plotting the target amplitude for a five peak Gaussian target PMF. 55

6.3 Target vs approximate amplitude for a target PMF with five Gaussian peaks. In the zoomed in plot we see how the tracking amplitude cannot accurately approximate the target due the oscillations being too large. 56

6.4 Comparing the approximate vs target PMF while varying the number of domains and keeping the length fixed. 57
6.5 Comparing the PMF and amplitude for $N = 1000$ and $N = 6000$. 58
6.6 Schematic of the main sources of error when ferroelectrically poling a crystal. 60
6.7 Comparing the approximate nonlinearity (top) to five sets of randomized errors. 61
6.8 Comparing the target amplitude, the approximate amplitude and five trials of the random error nonlinearity 62
6.9 Comparing the target PMF, approximate PMF and the PMF from the five random error nonlinearity profiles. 62

A.1 Plotting the amplitude throughout the crystal of a Gaussian target PMF with two different pre-factors. We can see that when we exceed the restriction of the slope of the target amplitude of $2/\pi$ we can no longer approximate the target. 74

B.1 Non linearity profile for a target Gaussian PMF. 76
B.2 Comparing the target amplitude to the approximate amplitude for a Gaussian target PMF 77
B.3 Gaussian centered at Δk_0 compared to engineered PMF 77
B.4 Plotting the JSA, PMF (lower plot) and pump (upper plot). 78

Chapter 1

Introduction

Quantum light is an important ingredient in emerging quantum technologies. It can be easily sent from one location to another, making it ideal for quantum communication [3] and quantum cryptography [4]. It can also posses desirable quantum properties, such as, superposition and entanglement, making it a good candidate for quantum information processing, either as a link between other quantum systems such as ion traps [5] or used directly for quantum computation [6]. Quantum light also has applications in imaging [7] and metrology [8].

In quantum optics, it is typical to classify states of light as "discrete variables", e.g. Fock states, or "Continuous variable" such as electric field eigenstates. An interesting class of continuous variable quantum states of light are Gaussian states, which satisfy the condition that the Wigner function, a quantum mechanical generalization of a phase-space probability distribution, is always positive [9]. Gaussian states can be used for quantum information protocols with the addition of a single nonlinear process, such as, photo detection. Many linear-optical transformations are Gaussian transformations, which take Gaussian states to Gaussian states. These two useful properties have led to a large theoretical toolbox which uses Gaussian states and photo detection for many continuous variable quantum information protocols [10].

Two common Gaussian states are single- and two-mode squeezed states [11]. The squeezing property of single-mode squeezed states makes them useful for quantum metrology [8]. Two-mode squeezed states are entangled states of the electromagnetic field, and can be used for quantum teleportation [3] and cryptography [4]. In this thesis we consider two generalizations of single- and two-mode squeezed states: (i) a class of states we call "tuneable hybrid squeezed states", and (ii) a class of states known as "multimode squeezed

states".

Hybrid states may posses the best of both single- and two-mode squeezed states. Their tuneable nature could be used to benefit quantum information protocols by having extra parameters that can be varied during an experiment. Multimode squeezed states on the other hand, generalize entanglement to N-partite entangled states, which can generalize many quantum information protocols. Hybrid and multimode squeezed states can be used for multi-parameter quantum metrology [12], multi-channel quantum imaging [13] and multi-partite teleportation [14].

Hybrid squeezed states [1] were first described in [15], where they proposed using a beam splitter and two single-mode squeezed states to generate a hybrid squeezed state. The state was tuned by varying the squeezing parameters and the phase of the beam splitter. This idea was then expanded upon to the multi mode case in 1999 by P. van Loock and Samuel L. Braunstein [16], where they used N beam splitters and only one single-mode squeezed state. A new method was proposed by [17], which used a continuous-wave source and an optical parametric oscillator to compactly generate four-mode squeezed states. This method was further generalized by [18] to generate many mode squeezed states from a continuous wave source.

In this thesis we propose and investigate a method to generate hybrid squeezed states, where the squeezing parameters can be tuned in real time. We then adapt our method to multimode squeezed states. Our method uses a spontaneous parametric process with a spectrally engineered pump and custom-engineered nonlinear crystal. What sets our work apart from the previous work is that the modes of the field are Gaussian frequency distributions which provides three advantages. The first advantage is that unlike the method proposed by [16, 17, 18], the states we generate are localized in time and frequency, allowing for high dimensional encoding that are compatible with waveguides and fiber transmission [19]. The second advantage is unlike the localized time-frequency modes of the Schmidt decomposition [19] which are hard to experimentally distinguish [20], our modes are defined by Gaussian distributions at center frequencies, making them easy to experimentally distinguish. Lastly, the states generated in [15, 16] relied on beam splitters to generate entangled states in the spatial modes of the field, whereas ours are in the same spatial mode which makes the experiment more stable. Our method can be scaled to many modes and the entangled states are all simultaneously available.

This thesis is structured as follows. In Chapter 2 we develop the theory of linear- and nonlinear-optics and detail an algorithm used to design custom-engineered nonlinear crystals with specified properties. We then define modes of the electromagnetic field

[1] originally called "two-mode squeezed gaussons"

as Gaussian frequency distributions and show that we can encode single- and two-mode squeezed states with this method in Chapter 3. We then propose a method for generating tuneable hybrid states in Chapter 4, by custom-shaping the spectral distribution of the input light and custom-engineering of the nonlinearity profile of the crystal. In Chapter 5 we adapt this method to generate squeezed states with many modes. We then discuss some limitations of our method and errors associated with it in Chapter 6. Finally, we conclude the work of this thesis in Chapter 7.

Chapter 2

Theory

In this chapter we introduce the necessary theoretical background to follow the rest of the work in this thesis. We begin with a section on classical optics and then quantize the electromagnetic (EM) field, we then review linear-optical transformations, including polarizing beam splitters, half-wave plates and beam splitters. We then introduce a nonlinear-optical process, known as spontaneous parametric downconversion (SPDC), and show how it can be used to generate various squeezed states of light. Finally, we discuss various methods used to customize the properties of squeezed light generated via SPDC, namely, group velocity matching, quasi phasematching, and customized nonlinearity shaping.

2.1 Quantization of Light in a Linear Material

2.1.1 Classical Optics

To quantize the EM field, we begin with the field's classical equations of motion. This approach closely follows the work in [21]. The derivation is quite involved, so here we only highlight the key points. We begin with Maxwell's equations for the displacement field

$\boldsymbol{D}(\boldsymbol{r})$ and magnetic field $\boldsymbol{B}(\boldsymbol{r})$ in a non-magnetic material, given by

$$\begin{aligned} \nabla \cdot \boldsymbol{D}(\boldsymbol{r}) &= 0 \\ \nabla \cdot \boldsymbol{B}(\boldsymbol{r}) &= 0 \\ -i\omega \boldsymbol{B}(\boldsymbol{r}) &= -\nabla \times \left(\frac{\boldsymbol{D}(\boldsymbol{r})}{\epsilon_0 n^2(x,y;\omega)} \right) \\ -i\omega \boldsymbol{D}(\boldsymbol{r}) &= \nabla \times \left(\frac{\boldsymbol{B}(\boldsymbol{r})}{\mu_0} \right). \end{aligned} \tag{2.1}$$

In Eq. (2.1) we assumed that the fields vary harmonically with frequency ω, that the direction of propagation is along z, and that the refractive index ($n^2(x,y;\omega)$) is only dependent on the orthogonal directions x, y, and ω. The solutions to the differential equations in (2.1) can be expanded in plane wave solutions along the direction of propagation. The displacement and magnetic fields are then given by

$$\begin{aligned} \boldsymbol{D}(\boldsymbol{r},t) &= \frac{1}{\sqrt{2\pi}} \sum_I \int dk \alpha_I(k) \boldsymbol{d}_{Ik}(x,y) e^{ikz - i\omega_{Ik}} + c.c. \\ \boldsymbol{B}(\boldsymbol{r},t) &= \frac{1}{\sqrt{2\pi}} \sum_I \int dk \alpha_I(k) \boldsymbol{b}_{Ik}(x,y) e^{ikz - i\omega_{Ik}} + c.c., \end{aligned} \tag{2.2}$$

where the sum is over another index of the field, $\alpha_I(k)$ are the amplitudes of each mode, $\boldsymbol{r}$ is the location where the field is being evaluated, and $\boldsymbol{d}_{Ik}(x,y)$,$\boldsymbol{b}_{Ik}(x,y)$ characterizes the mode profile for the displacement and magnetic field respectively. We choose a conventional normalization for the transverse direction of the field given in [22].

$$\int dxdy \frac{\boldsymbol{d}^*_{Ik}(x,y) \cdot \boldsymbol{d}_{Ik}(x,y)}{\epsilon n^2(x,y;\omega_{Ik})} \frac{v_p(x,y;\omega_I k)}{v_g(x,y;\omega_I k)} = 1, \tag{2.3}$$

where v_p and v_g are the local phase and group velocity in the medium.

2.1.2 Quantizing the Classical Electromagnetic Field

To quantize the EM field we now promote the amplitudes $\alpha_I(k)$ into operators $\hat{a}_I(k)$. In the Schrödinger picture, the field operators are then given by

$$\begin{aligned} \hat{\boldsymbol{D}}(\boldsymbol{r}) &= \sum_I \int dk \sqrt{\frac{\hbar\omega_{Ik}}{2}} \hat{a}_I(k) \boldsymbol{d}_{Ik}(x,y) e^{ikz} + H.c. \\ \hat{\boldsymbol{B}}(\boldsymbol{r}) &= \sum_I \int dk \sqrt{\frac{\hbar\omega_{Ik}}{2}} \hat{a}_I(k) \boldsymbol{b}_{Ik}(x,y) e^{ikz} + H.c.. \end{aligned} \tag{2.4}$$

The creation and annihilation operators then satisfy the two commutation relations

$$[\hat{a}_I(k), \hat{a}_{I'}(k')] = 0, \qquad \left[\hat{a}_I(k), \hat{a}^\dagger_{I'}(k')\right] = \delta_{II'}\delta(k-k'). \tag{2.5}$$

The Hamiltonian for the EM field in a linear material is given by

$$\hat{H} = \int d^3x \left(\hat{\mathbf{E}} \cdot d\hat{\mathbf{D}} + \frac{1}{\mu_0}\hat{\mathbf{B}} \cdot d\hat{\mathbf{B}}\right), \tag{2.6}$$

after substituting in the equations for the field in (2.4) we arrive at the linear Hamiltonian given by

$$\hat{H}_L = \sum_I \int dk \omega_{Ik} \hat{a}^\dagger_I(k)\hat{a}_I(k). \tag{2.7}$$

The operators $\hat{a}^\dagger_I(k)$ and $\hat{a}_I(k)$ can be used to write down interesting quantum states of light, which we introduce in the next section.

2.1.3 Quantum States of Light

Quantum states of light are useful in many quantum information protocols such as quantum teleportation, quantum metrology, and quantum cryptography. In this section we assume we have a single mode of the field and therefore drop the index I and k for clarity.

We begin with coherent states of light [23]. A coherent state is described by

$$|\alpha\rangle = e^{\alpha^* a^\dagger - H.c.} |0\rangle, \tag{2.8}$$

where α is a complex number that defines the phase and amplitude of the state. Coherent states have the property that they minimize the quantum uncertainty and the field expectation value oscillates sinusoidally. Coherent states are important because they are used to model the output of a laser [24] and can be used to encode information for continuous variable quantum computing. One way to use coherent states for quantum computation is to encode the logical qubits as $|0\rangle = |\alpha\rangle$ and $|1\rangle = |-\alpha\rangle$ [25].

The next set of states that are often used for quantum information protocols are squeezed states. There are many types of squeezed states [26], but we will focus on single-mode squeezed vacuum (SMSV) and two-mode squeezed vacuum (TMSV) states.

A SMSV state is given by [23]

$$|\text{SMSV}\rangle = e^{\frac{\beta^*}{2}\hat{a}^\dagger\hat{a}^\dagger - H.c.} |0\rangle \tag{2.9}$$

where β is a complex number called the squeezing parameter that controls the amount and phase of the squeezing. A SMSV state is classified as single-mode because there is only one mode of the field in the exponential, it is squeezed due to it being quadratic in creation/annihilation operators in the exponential, and a vacuum state because the expectation value of the field is zero. Due to the squeezing property of SMSV states, they have found applications in the field of quantum metrology [8].

TMSV states are define in a similar way given by [23]

$$|\text{TMSV}\rangle = e^{\frac{\gamma^*}{2}\hat{a}^\dagger\hat{b}^\dagger - H.c.}\,|0\rangle\,, \tag{2.10}$$

where again, γ is a complex number called the squeezing parameter. A TMSV state has two modes of the field in the exponential. These two modes are typically either two orthogonal polarizations or two spatial degrees of freedom. Similar to a SMSV state, a TMSV state is quadratic in field operators and has a field expectation value of zero. TMSV states are entangled states of the EM field and in the limit of infinite squeezing, the state is equal to an Einstein-Podolsky-Rosen state [27]. Due to the entanglement of TMSV states, they are ideal for continuous variable quantum teleportation, quantum dense coding and quantum cryptography, all which use entanglement to there advantage [28, 29, 4].

2.2 Linear Optics

Linear optics and linear-optical transformations manipulate the degrees of freedom of quantum states of light, such as polarization, phase, and spatial/temporal locations. Linear optics includes the application of mirrors, wave plates, polarizing beam splitters and beam splitters. In this section we discuss these linear-optical devices.

2.2.1 Polarizing Beam Splitter

A polarizing beam splitter is a linear-optical device that can separate the polarization degree of freedom from incident light. Light incident onto a polarizing beam splitter will be separated into two spatial modes each with an orthogonal polarization. The polarizing

beam splitter transformations are given by [30]

$$\begin{aligned}
\hat{U}_{PBS}\hat{a}_H^{(1)}\hat{U}_{PBS}^\dagger &= \hat{a}_H^{(1')} \\
\hat{U}_{PBS}\hat{a}_V^{(1)}\hat{U}_{PBS}^\dagger &= \hat{a}_V^{(2')} \\
\hat{U}_{PBS}\hat{a}_H^{(2)}\hat{U}_{PBS}^\dagger &= \hat{a}_H^{(1')} \\
\hat{U}_{PBS}\hat{a}_V^{(2)}\hat{U}_{PBS}^\dagger &= \hat{a}_V^{(2')},
\end{aligned} \tag{2.11}$$

where the superscript (1) and (2) denote the spatial degree of freedom in paths 1 and 2.

2.2.2 Half-Wave Plate

A wave plate is an optical element (usually a birefringent material) that transforms the polarization of light. In this work we will be interested in half-wave plates. If we label the modes $\hat{a}_H$ and mode $\hat{a}_V$ as being horizontal and vertical polarized modes, then a half-wave plate at an angle φ (where φ is the angle between the incident light polarization and the fast axis of the half-wave plate) acting on these modes is given by [31],

$$\begin{aligned}
U_{HWP}(\varphi)a_H U_{HWP}^\dagger(\varphi) &= \cos(2\varphi)\hat{a}_H + i\sin(2\varphi)\hat{a}_V \\
U_{HWP}(\varphi)\hat{a}_V U_{HWP}^\dagger(\varphi) &= i\sin(2\varphi)\hat{a}_H + \cos(2\varphi)\hat{a}_V.
\end{aligned} \tag{2.12}$$

If we set the angle $\varphi = \pi/4$, then the half-wave plate will rotate horizontally polarized light to vertically polarized light while also picking up a phase of $\pi/2$.

2.2.3 Beam Splitter

A beam splitter is one of the easiest ways to mix two modes of an EM field. In this thesis we will consider two different spatial modes with different frequency distributions. We can apply the following transformations to the above modes because the transformation is linear. That is, we can act the transformation on each frequency independently. Consider two modes of an EM field incident on a beam splitter, the unitary transformation of the beam splitter on the two modes is given by [30],

$$\begin{aligned}
U_{BS}\hat{a}U_{BS}^\dagger &= \hat{c} = t\hat{a} + re^{i\theta_1}\hat{b} \\
U_{BS}\hat{b}U_{BS}^\dagger &= \hat{d} = re^{i\theta_2}\hat{a} + t\hat{b},
\end{aligned} \tag{2.13}$$

where t is the complex transmission and r is the complex reflection coefficients. Preserving the commutation relations of the new modes $\hat{c}$ and $\hat{d}$, one finds that r and t must satisfy

$$|t|^2 + |r|^2 = 1, \tag{2.14}$$

$$t^* r e^{i\theta_1} + t r^* e^{-i\theta_2} = 0. \tag{2.15}$$

In this thesis, we will only be interested in a 50:50 beam splitter, that is $t = r = \frac{1}{\sqrt{2}}$, then $\theta_1 + \theta_2 = \pi$. Setting $\theta_2 = \theta$, the beam splitter transformations are given by

$$\begin{aligned} \hat{a} \to U_{BS} \hat{a} U_{BS}^\dagger &= \frac{1}{\sqrt{2}}(\hat{a} + e^{i\theta}\hat{b}) \\ \hat{b} \to U_{BS} \hat{b} U_{BS}^\dagger &= \frac{1}{\sqrt{2}}(-e^{-i\theta}\hat{a} + \hat{b}). \end{aligned} \tag{2.16}$$

2.3 Nonlinear Optics

When EM waves pass through a material they interact with the material's atoms. The EM field induces a polarization into the material that alters the EM field itself. A material has a nonlinear response to EM fields when the polarization depends on higher powers of the displacement field.

In this thesis we will focus on an nonlinear-optical process that involves the interaction of three fields. This process is known as spontaneous parametric downconversion (SPDC).

2.3.1 Spontaneous Parametric Down conversion

SPDC is a nonlinear process when light interacts with a crystal with a second-order nonlinearity, denoted as $\chi_{(2)}$. In a SPDC process the input photons, typically called pump photons, are each "downconverted" into two daughter photons, called the signal and idler. The signal and idler photons satisfy energy and momentum conservation with the pump photon given by

$$\omega_p = \omega_s + \omega_i, \qquad k_p(\omega_p) = k_s(\omega_s) + k_i(\omega_i) \tag{2.17}$$

where ω_j and $k_j(\omega_j)$ are the frequency and wave vectors. The three fields of interest are labeled by $j = p, s, i$, denoting the pump, signal and idler respectively. If we simplify the problem so that the interaction occurs in a 1D wave guide the schematic of a Type II SPDC process is given by figure 2.1.

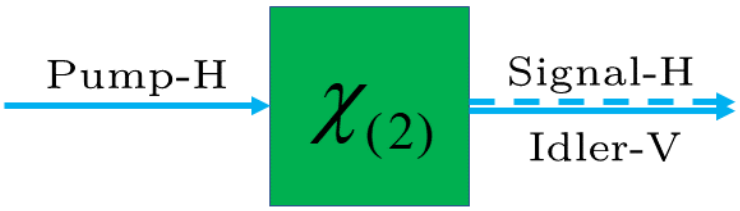

Figure 2.1: Schematic of a Type 2 SPDC process in a 1D wave guide. The pump photon is downconverted into two orthogonally polarized photons denoted signal and idler. The pump and signal photon is horizontally polarized and the idler is vertically polarized. The process is mediated by a crystal with a $\chi_{(2)}$ nonlinearity and is energy and momentum conserving.

We now provide a detailed derivation of a SPDC process, followed from the work in [21]. We begin by expanding the polarization of the material in a power series of the displacement operator

$$\hat{P}^i(\boldsymbol{r},t) = \Gamma^{ij}_{(1)}(\boldsymbol{r})\hat{D}^j(\boldsymbol{r},t) + \Gamma^{ijk}_{(2)}\hat{D}^j(\boldsymbol{r},t)\hat{D}^k(\boldsymbol{r},t) + ..., \tag{2.18}$$

then the second-order nonlinear contribution to the Hamiltonian is given by

$$\hat{H}_{NL} = -\frac{1}{3\epsilon_0}\int_V d^3x \Gamma^{ijk}_{(2)}(\boldsymbol{r})\hat{D}^i(\boldsymbol{r},t)\hat{D}^j(\boldsymbol{r},t)\hat{D}^k(\boldsymbol{r},t) + ... \tag{2.19}$$

We now labeling the three field operators by p,s,i and switch to the more commonly used nonlinear tensor $\chi_{(2)}(\boldsymbol{r})$ given by

$$\Gamma^{ijk}_{(2)}(\boldsymbol{r}) \to \frac{\chi^{ijk}_{(2)}(\boldsymbol{r})}{\epsilon_0 n^2(\boldsymbol{r};\omega_{k_p})n^2(\boldsymbol{r};\omega_{k_i})n^2(\boldsymbol{r};\omega_{k_s})}. \tag{2.20}$$

Then for a Type II downconversion process, in the rotating wave approximation, assuming the material is in an effective 1D structure where the field doesn't vary in the orthogonal direction of area A, after mode expanding $\hat{\mathbf{D}}(\boldsymbol{r},t)$ according to Eq. (2.4), and substituting $k_j(\omega_j) = \omega_j n_j(\omega_j)/c$ the nonlinear Hamiltonian in the interaction picture is

$$\begin{aligned}\hat{H}_I(t) = &-\hbar\int_0^\infty d\omega_p d\omega_i d\omega_s \hat{c}_V(\omega_p)\hat{a}^\dagger_V(\omega_i)\hat{a}^\dagger_H(\omega_s)e^{i(\omega_s+\omega_i-\omega_p)t}\mathcal{A}(\omega_p,\omega_s,\omega_i)\times \\ &\int_{-L/2}^{L/2} dz g(z)e^{i(k_p(\omega_p)-k_i(\omega_i)-k_s(\omega_s)z} + H.c.,\end{aligned} \tag{2.21}$$

with

$$\mathcal{A}(\omega_p, \omega_s, \omega_i) = 2\chi_{(2)}\sqrt{\frac{\omega_p \hbar\omega_i \hbar\omega_s}{\hbar(4\pi)^3\epsilon_0 A c^3 n_p(\omega_p) n_s(\omega_s) n_i(\omega_i)}}, \tag{2.22}$$

and

$$g(z) = \frac{\chi_{(2)}(z)}{\chi_{(2)}}. \tag{2.23}$$

Where $g(z)$ is the nonlinearity profile of the crystal with magnitude 1 and the photons are generated in orthogonal polarizations. The physical picture to imagine is that a photon at frequency ω_p enters the nonlinear crystal at $z = -L/2$, it is then downconverted into two photons at frequencies ω_i and ω_s which then exit the crystal at $z = L/2$.

2.3.2 The Downconverted State

In the interaction picture the states evolves according to interaction Hamiltonian given by [32]

$$i\hbar\frac{d\left|\psi(t)\right\rangle}{dt} = \hat{H}_I(t)\left|\psi(t)\right\rangle, \tag{2.24}$$

which has a formal solution of

$$\left|\psi_{out}\right\rangle = T[e^{\frac{-i}{\hbar}\int_{-\infty}^{\infty} dt\hat{H}_I(t)}]\left|\psi_{in}\right\rangle, \tag{2.25}$$

where T is the time-ordering operator and the states $|\psi_{in}\rangle$ and $|\psi_{out}\rangle$ are the states in the infinite past and infinite future respectively. Since the interaction Hamiltonian does not commute with itself at different times, we cannot in general drop the time ordering operator. It was shown in [33], that the time ordering leads to non trivial effects but only in the high pump power regime. For this work, we will assume low pump powers and not worry about these time ordering effects, i.e. we drop the time-ordering operator.

Integrating the above interaction Hamiltonian with respect to t we find

$$\begin{aligned}\left|\psi_{out}\right\rangle = \exp\Bigg(i\int_0^{\infty} d\omega_p d\omega_i d\omega_s \hat{c}_V(\omega_p)\hat{a}_V^{\dagger}(\omega_i)\hat{a}_H^{\dagger}(\omega_s)\delta(\omega_s+\omega_i-\omega_p)\mathcal{A}(\omega_p,\omega_s,\omega_i) \\ \int_{-L/2}^{L/2} dz g(z)e^{i\Delta kz} + H.c.\Bigg)\left|\psi_{in}\right\rangle,\end{aligned} \tag{2.26}$$

where the integral over t produced an energy conserving term $\delta(\omega_s+\omega_i-\omega_p)$ and we refer to $\Delta k(\omega_p, \omega_i, \omega_s) = k_p(\omega_p) - k_i(\omega_i) - k_s(\omega_s)$ as the *phase mismatch*.

2.3.3 The Pump Function

If we take the input state to be a coherent state and the signal and idler in the vacuum state $|\psi_{in}\rangle = |0_s 0_i \alpha_p\rangle$, then in the undepleted pump approximation (where we assume the pump light is unchanged with the removal of a photon) we can simplify the above output state as

$$|\psi\rangle = \exp\left(i \int_0^\infty d\omega_i d\omega_s \textsc{pump}(\omega_p) \hat{a}_V^\dagger(\omega_i) \hat{a}_H^\dagger(\omega_s) \mathcal{A}(\omega_s, \omega_i) \int_{-L/2}^{L/2} dz g(z) e^{i\Delta k(\omega_s, \omega_i) z} + H.c. \right) |0\rangle , \tag{2.27}$$

where the function $\textsc{pump}(\omega_p)$ is the frequency distribution of the input light.

2.3.4 The Phasematching Function

We define the phasematching function (PMF) by

$$\textsc{pmf}(\omega_s, \omega_i) = \int_{-L/2}^{L/2} dz g(z) e^{i\Delta k(\omega_s, \omega_i) z}. \tag{2.28}$$

2.3.5 The Joint Spectral Amplitude

Integrating over ω_p and evaluating $\delta(\omega_s + \omega_i - \omega_p)$ the output state is given by

$$|\psi_{out}\rangle = \exp\left(i \int_0^\infty d\omega_i d\omega_s \textsc{pump}(\omega_s + \omega_i) \hat{a}_V^\dagger(\omega_i) \hat{a}_H^\dagger(\omega_s) \mathcal{A}(\omega_s, \omega_i) \textsc{pmf}(\omega_s, \omega_i) + H.c. \right) |\psi_{in}\rangle . \tag{2.29}$$

We define the joint spectral amplitude (JSA) as

$$\textsc{jsa}(\omega_s, \omega_i) = \mathcal{A}(\omega_s, \omega_i) \times \textsc{pump}(\omega_s + \omega_i) \times \textsc{pmf}(\Delta k(\omega_s, \omega_i)), \tag{2.30}$$

which is the spectral distribution of the generated photons. We then extend the bounds of integration to $-\infty$, since there are no contributions to the integral in that region. Therefore, for a Type II SPDC process, via a crystal with a nonlinearity profile given by $g(z)$, in the rotating wave and undepleted pump approximation, the output state of light is given by

$$|\psi\rangle = \exp\left(i \int d\omega_i d\omega_s \textsc{jsa}(\omega_s, \omega_i) \hat{a}_H^\dagger(\omega_i) \hat{a}_V^\dagger(\omega_s) + H.c. \right) |0\rangle . \tag{2.31}$$

Suppose we could decompose the JSA as

$$\text{JSA}(\omega_s, \omega_i) = \gamma f(\omega_s) g(\omega_i), \tag{2.32}$$

where f and g are functions of a single variable.The JSA might schematically be given by Fig. 2.2, where in this case the JSA is symmetric and $f(\omega) = g(\omega)$. For the JSA in Fig. 2.2 we can define the operators

$$\begin{aligned} \hat{F}_H^\dagger &= \int d\omega f(\omega) \hat{a}_H^\dagger(\omega) \\ \hat{F}_V^\dagger &= \int d\omega g(\omega) \hat{a}_V^\dagger(\omega), \end{aligned} \tag{2.33}$$

inputting them into Eq. (2.31) we find

$$|\psi\rangle = e^{i\gamma \hat{F}_H^\dagger \hat{F}_V^\dagger + H.c.} |0\rangle . \tag{2.34}$$

Notice that this is exactly the TMSV state that was defined in Eq. (2.10), if the two modes were taken to be orthogonal polarizations. Here we see that the output of a SPDC process is a two mode squeezed state when we can decompose the JSA as in Eq. 2.32.

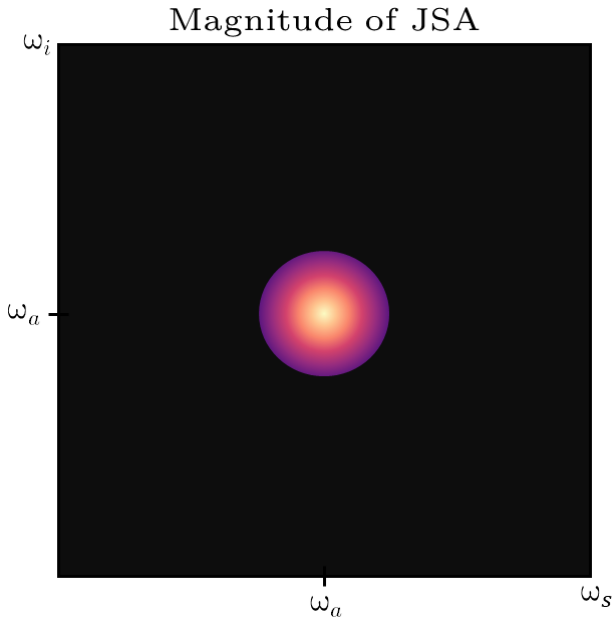

Figure 2.2: Schematic drawing of a JSA for a typical SPDC process.

For a typical SPDC process, however, the JSA might look like Fig. 2.3. In this case, the JSA cannot be decomposed by two single functions, we instead rely on the Schmidt decomposition [34]. For any 2D function, the Schmidt decomposition in given by

$$\text{JSA}(\omega_i, \omega_s) = \sum_n \sqrt{p_n} u_n(\omega_s) v_n(\omega_i), \tag{2.35}$$

where for a normalized JSA, the constants p_n satisfy the properties of a discrete probability distribution and the functions u_n, v_n satisfy

$$\begin{aligned} \int d\omega_s u_n^*(\omega_s) u_m(\omega_s) &= \delta_{nm} \\ \int d\omega_i v_n^*(\omega_i) v_m(\omega_i) &= \delta_{nm}. \end{aligned} \tag{2.36}$$

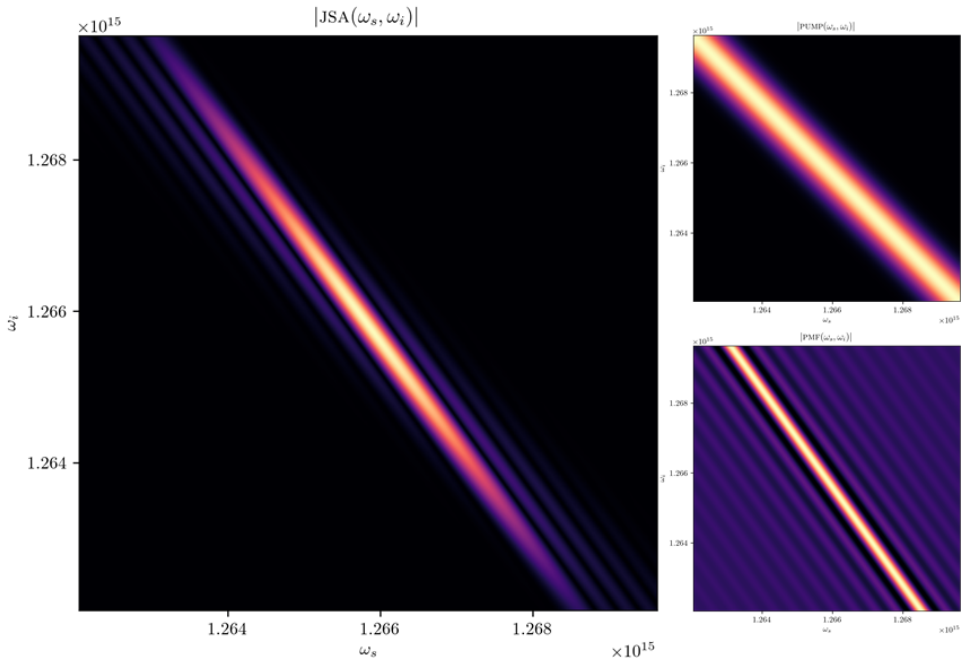

Figure 2.3: Typical pump,PMF and JSA for a SPDC process.

Then defining the operators

$$\begin{aligned}\hat{U}^{\dagger}_{H,n} &= \int d\omega u_n(\omega)\hat{a}^{\dagger}_H(\omega) \\ \hat{V}^{\dagger}_{V,n} &= \int d\omega v_n(\omega)\hat{a}^{\dagger}_V(\omega),\end{aligned} \tag{2.37}$$

the output of the SPDC process in Eq. (2.31) can be written as

$$|\psi\rangle = e^{i\sum_n \sqrt{p_n}\hat{U}^{\dagger}_{H,n}\hat{V}^{\dagger}_{V,n}+H.c.}|0\rangle\,. \tag{2.38}$$

In Eq (2.38), every mode is orthogonal to each other due to the orthogonality of the functions u_n, v_n and the orthogonality of the polarization, therefore every operator commutes. We can then break up the sum in the exponential of Eq. (2.38) into a product state given by

$$|\psi\rangle = \bigotimes_n e^{i\sqrt{p_n}\hat{U}^{\dagger}_{H,n}\hat{V}^{\dagger}_{V,n}+H.c.}|0\rangle \tag{2.39}$$

which is a product of TMSV states.

2.4 Properties of the Phasematching Function

The JSA can be customized via the pump function or the PMF. In this thesis, we assume that methods for customizing the pump function exist, and focus on customizing the PMF. In this section we describe some key features of the PMF. The PMF was defined as

$$\text{PMF}(\omega_s,\omega_i) = \int_{-L/2}^{L/2} dz g(z) e^{i\Delta k(\omega_s,\omega_i)z}, \tag{2.40}$$

where $g(z)$ is the nonlinearity profile along the crystal and $\Delta k(\omega_s,\omega_i)$ is the phase mismatch. In principle, one can imagine varying $g(z)$ continuously. Such methods, however, don't exist for nonlinear crystals. In practice, the nonlinearity profile for a crystal can only be $g(z) = \pm 1$ [35]. We will now consider the simplest case, where the nonlinearity profile is constant throughout the crystal.

2.4.1 Uniform Crystal

For a uniform crystal with a constant nonlinearity (i.e. $g(z) = 1$ inside the crystal) the PMF is given by

$$\begin{aligned} \text{PMF}(\omega_s, \omega_i) &= \int_{-L/2}^{L/2} dz e^{i\Delta k(\omega_s,\omega_i)z} \\ &= L\,\text{sinc}\left(\frac{\Delta k(\omega_s,\omega_i)L}{2}\right). \end{aligned} \tag{2.41}$$

For a uniform crystal, the PMF peaks at $\Delta k = 0$, which is the manifestation of momentum conservation. We call this regime "phase match". Expanding the phase mismatch by using the equation $k_j(\omega_j) = \omega_j n_j(\omega_j)/c$ where c is the speed of light in vacuum we find

$$\begin{aligned} \Delta k(\omega_s, \omega_i) &= k_p(\omega_s + \omega_i) - k_s(\omega_s) - k_i(\omega_i) \\ &= \frac{(\omega_s + \omega_i)n_p(\omega_s + \omega_i)}{c} - \frac{\omega_s n_s(\omega_s)}{c} - \frac{\omega_i n_i(\omega_i)}{c}. \end{aligned} \tag{2.42}$$

For a Potassium Titanyl Phosphate (KTP) crystal, the refractive index $n(\omega)$ is an increasing function of frequency, so the phasematching condition cannot be achieved for any set of signal and idler frequencies [35]. To generate photons, we need to design the crystal to be quasi-phasematched which will be the topic of Sec 2.4.3.

2.4.2 Group Velocity Matching

In Eq. (2.41) we calculated the PMF for a uniform crystal which can be plotted as a function of ω_s and ω_i. In this thesis we are interested in the regime where the PMF intersects the pump in a narrow frequency range. We can therefore Taylor expand the phase mismatch to first order by

$$k_j(\omega_j) = k_j(\Omega_j) + \left.\frac{dk_j(\omega_j - \Omega_j)}{d\omega_j}\right|_{\Omega_j}. \tag{2.43}$$

Inputting the Taylor expansions into the phase mismatch

$$\begin{aligned}\Delta k(\omega_s,\omega_i) &= k_p(\Omega_s+\Omega_i) + \left.\frac{dk_p(\omega_s+\omega_i-(\Omega_s-\Omega_i))}{d(\omega_s+\omega_i)}\right|_{\Omega_s+\Omega_i} - k_s(\Omega_s) \\ &- \left.\frac{dk_s(\omega_s-\Omega_s)}{d\omega_s}\right|_{\Omega_s} - k_i(\Omega_i) - \left.\frac{dk_i(\omega_i-\Omega_i)}{d\omega_i}\right|_{\Omega_i} \\ &= \Delta k_0 + \left.\frac{dk_p(\omega_s+\omega_i-(\Omega_s+\Omega_i))}{d(\omega_s+\omega_i)}\right|_{\Omega_s+\Omega_i} - \left.\frac{dk_s(\omega_s-\Omega_s)}{d\omega_s}\right|_{\Omega_s} \\ &- k_i(\Omega_i) - \left.\frac{dk_i(\omega_i-\Omega_i)}{d\omega_i}\right|_{\Omega_i},\end{aligned} \tag{2.44}$$

where $\Omega_p = \Omega_s + \Omega_i$ and $\Delta k_0 = k_p(\Omega_p) - k_s(\Omega_s) - k_i(\Omega_i)$.

To evaluate $k_j(\Omega_j)$ we need to make use of the equation $k_j(\omega_j) = \omega_j n_j(\omega_j)/c$ and Sellmeier's equation [36]. Sellmeier's equation is an empirical relationship between the refractive index of a material as a function of the wavelength of light in vacuum. The relationship is given by

$$n(\lambda) = \sqrt{A_1 + \frac{A_2}{\lambda^2 - A_3} - A_4\lambda^2}, \tag{2.45}$$

for some set of constants A_1, A_2, A_3, A_4, which depend on the material and lights polarization, they are usually quoted for λ measured in μm where λ is given by $\lambda = 2\pi c/\omega$.

We now define $dk_j/d\omega_j|_{\Omega_j} = 1/v_j$ where v_j is the group velocity in the crystal for mode j. Then defining the variable $\bar{\omega}_j = \omega_j - \Omega_j$ which lets us rewrite the phase mismatch as

$$\Delta k(\bar{\omega}_s,\bar{\omega}_i) = \Delta k_0 + \left(\frac{1}{v_p} - \frac{1}{v_s}\right)\bar{\omega}_s + \left(\frac{1}{v_p} - \frac{1}{v_i}\right)\bar{\omega}_i. \tag{2.46}$$

The first order terms in the phase mismatch lead to rotations of the PMF by an angle θ given by

$$\tan\theta = -\left(\frac{1}{v_p} - \frac{1}{v_s}\right) \Big/ \left(\frac{1}{v_p} - \frac{1}{v_i}\right) \tag{2.47}$$

In Fig. 2.4 we plot the PMF for different group velocities. In this thesis, we will be interested in the case where the PMF is perpendicular to the pump.

2.4.3 Quasi Phasematching

In the above section we took a nonlinear crystal with a uniform nonlinearity function set to $g(z) = +1$ for the whole length of the crystal. This led to a PMF that was peaked at

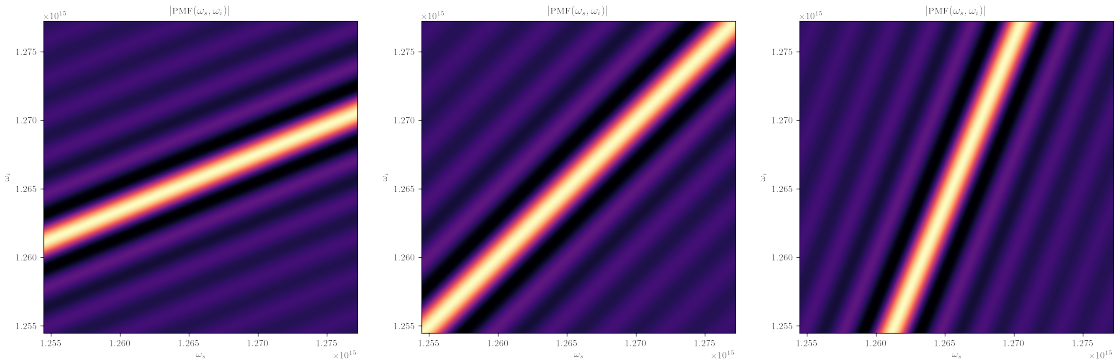

(a) PMF at an angle of $\theta = 22.5°$.

(b) PMF at an angle of $\theta = 45°$.

(c) PMF at an angle of $\theta = 67.5°$.

Figure 2.4: PMF for a uniform nonlinear crystal with different group velocities.

$\Delta k = 0$ but in practice for a KTP crystal, we cannot achieve phasematching at practical frequencies. What we do instead is introduce a grating into the nonlinearity which adds an additional momentum component to the system, effectively shifting the peak of the phasematching function. In practice we do this by varying the nonlinearity between ± 1 through the crystal periodically. For a given phase mismatch Δk_0, we can define the oscillation period by $\Lambda = 2\pi/\Delta k_0$ then by flipping the nonlinearity every $\Lambda/2$ we can shift the peak of the PMF to $\Delta k_0 = 2\pi/\Lambda$ [37].

2.4.4 Ferroelectric Poling

Ferroelectric Poling was first introduced by Yamada, M. et al. [38] in 1993. They proposed the method to quasi-phase-match a $LiNbO_3$ crystal. The polarization of ferroelectric materials can be permanently reversed by applying an external electric field [39]. By controlling the field, we can change the nonlinearity of the crystal from being $+1$ to -1.

This method can be done locally by applying a local electrode to the material. This allows us to change the nonlinearity within the crystal between $+1$ and -1 to our specification. In the region of the electrode the nonlinearity gradually switches sign and expands away from the electrode until the desired region is achieved. In Fig. 2.5 we show the process of reversing the nonlinearity by applying an electrode and in Fig. 2.4.4 show a real ferroelectrically poled crystal.

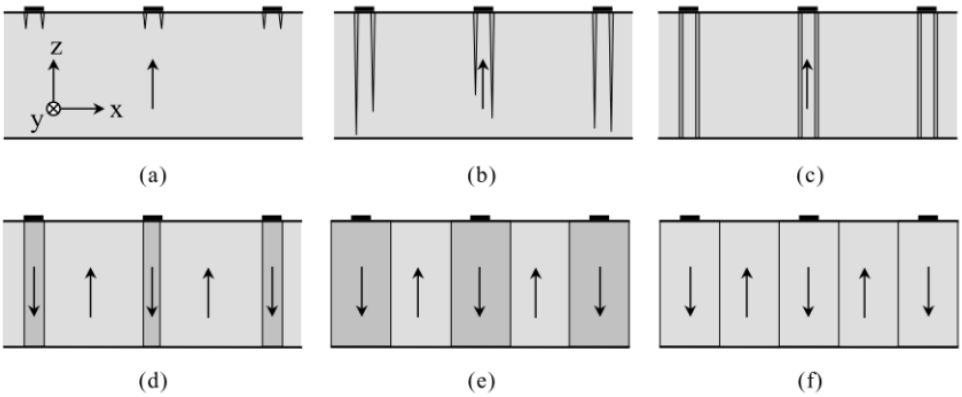

Figure 2.5: Showing how the nonlinearity in flipped by applied a field at a localized electrode. Figure was taken from [1].

Figure 2.6: Crystal that has been ferroelectrically poled. The different shades of grey correspond to a nonlinearity that is either $+1$ or -1. This figure was taken from [2] with permission.

2.4.5 Motivating a Tailored Phasematching Function

For classical optics, we are usually interested in generating SPDC photons with the highest amplitude achievable. For a KTP crystal, we can maximize the amplitude by quasi phasematching. This shifts the sinc shape PMF to the phase mismatch Δk_0 of the signal and idler photons. Since we are evaluating the PMF at the phase mismatch the shape of the PMF is not relevant for classical optical processes.

For quantum optical processes it turns out the shape of the PMF is very important in determining the properties of the output signal and idler photons, for example the purity of heralded single photons [40]. By designing nonlinear crystals, we can sacrifice some of the

amplitude of the PMF to change the shape so we can control the properties of the output photons. In this thesis we focus on the state of the art method of ferroelectric poling to tailor the nonlinearity profile of a crystal.

2.5 Nonlinearity Engineering

In section 2.4.4, we described ferroelectric poling which is a method used to change the nonlinearity of a nonlinear crystal so that the nonlinearity is either ± 1 in a localized way. The manipulation of individual domains led to a new branch of nonlinear optics which had the purpose of designing nonlinear crystal that would correspond to PMFs with desired properties.

The first method proposed in [2], which manipulated the nonlinearity at multiples of the coherence lengths $\Lambda/2$ while maintaining the ratio of domains with $g(z) = 1$ to $g(z) = -1$. The next method proposed by [41] kept each domain length to be the coherence length but customized the ratio of the percentage of poled vs unpoled regions. Later, approaches used simulated annealing to determine what the optimal nonlinearity profile should be [42]. They would first calculate the PMF and then change a domain and then looked at the output. Here we use a state-of-the-art method to track the amplitude of the PMF and determine the exact nonlinearity profile which was first used by [43] and then expanded upon by [44]. We will begin by revisiting the uniformly poled crystal.

2.5.1 Amplitude of a Uniform Crystal

This section makes use of the algorithm proposed in [44]. The approach we use here is to track the amplitude of the PMF within the crystal as a function of z and flip the nonlinearity accordingly. To track the PMF throughout the crystal we define the Amplitude by

$$A(z, \Delta k_0) = \int_{-L/2}^{z} dz' g(z') e^{i\Delta k_0 z'}, \tag{2.48}$$

which is the PMF evaluated at a given phase mismatch Δk_0 and as a function of z throughout the crystal. If we calculate the amplitude for a uniform crystal, which is when the

nonlinearity is constant throughout the crystal, we find

$$\begin{aligned} A(z, \Delta k_0) &= \int_{-L/2}^{z} dz' e^{i\Delta k_0 z'} \\ &= \frac{2}{\Delta k_0} \sin\left(\frac{\Delta k_0}{4}(2z + L)\right) e^{i\Delta k_0 (2z-L)/4}. \end{aligned} \tag{2.49}$$

Taking the real part and using trigonometric identities to simplify, we find

$$\begin{aligned} \Re(A(z, \Delta k_0)) &= \frac{1}{\Delta k_0} \sin\left(\frac{\Delta k_0}{4}(2z + L)\right) \cos\left(\frac{\Delta k_0}{4}(2z - L)\right) \\ &= \frac{\sin(\Delta k_0 L/2)}{\Delta k_0} + \frac{\sin(\Delta k_0 z)}{\Delta k_0}. \end{aligned} \tag{2.50}$$

The amplitude starts at zero when $z = -L/2$ and oscillates with a frequency of Δk_0. Again defining Λ, the period of oscillation, by $\Lambda = 2\pi/\Delta k_0$. For a uniform nonlinearity with a phase mismatch $\Delta k_0 \neq 0$, the amplitude cannot increase throughout the crystal. This is related to section 2.4.3 where it was shown that a PMF for a uniform crystal evaluated at a phase mismatch $\Delta k_0 \neq 0$ had a significantly reduced amplitude.

The amplitude oscillates with period Λ but increase and decreases over the coherence length given by $l_c = \Lambda/2$. If we could introduce a π phase shift at every coherence length the amplitude would constructively add throughout the crystal and increase. Adding a π phase shift at the end of every coherence length is equivalent to switching the nonlinearity between ± 1, the crystal would then be periodically polled.

By changing the nonlinearity between ± 1, we can control whether the amplitude is increasing or decreasing. To tailor a nonlinear crystal which has a target PMF we will take advantage of this property.

2.5.2 Algorithm for Tailoring a Nonlinear Crystal

We begin with a target PMF, this is a 1D function of the phase mismatch Δk. In Eq. (2.28) the PMF is related to the nonlinearity profile by the Fourier transform. We then inverse Fourier transform the target PMF to calculate the target nonlinearity. Using the target nonlinearity, we can calculate the target amplitude throughout the crystal. We then break the crystal into N pieces of length l_c so that $L = Nl_c$ is the length of the crystal. The algorithm then tracks the target amplitude and flips the nonlinearity between ± 1 depending on the result of a cost function in such a way that the actual crystal amplitude

approximates the target. After this process we then have a set of values for the nonlinearity over each coherence length. The final step is to use it to calculate the approximate PMF.

To simplify some notation we will use the function $\Phi_t(\Delta k)$, $\Phi_a(\Delta k)$, $A_t(z)$ and $A_a(z)$ to denote the target and approximate PMF and field amplitude respectively. This method can be summarized as:

1. Using Φ_t, calculate A_t.
2. Implement algorithm to track A_t and calculate $g_a(z)$.
3. Use $g_a(z)$ to calculate Φ_a.

For Step 1. we start with the target PMF,

$$\Phi_t(\Delta k) = \int_{-L/2}^{L/2} dz g_t(z) e^{i\Delta k z}, \tag{2.51}$$

then inverse Fourier transforming we have

$$g_t(z) = \frac{1}{2\pi} \int d(\Delta k) \Phi_t(\Delta k) e^{-i\Delta k z}, \tag{2.52}$$

inputting this into the equation for the field amplitude we find

$$\begin{aligned} A_t(\Delta k_0, z) &= \int_{-L/2}^{z} dz' g_t(z') e^{i\Delta k_0 z'} \\ &= \int_{-L/2}^{z} dz' \left(\frac{1}{2\pi} \int d(\Delta k) \Phi_t(\Delta k) e^{-i\Delta k z'} \right) e^{i\Delta k_0 z'} \\ &= \frac{1}{2\pi} \int d(\Delta k) \Phi_t(\Delta k) \int_{-L/2}^{z} dz' e^{i(\Delta k_0 - \Delta k) z'} \\ &= \frac{1}{\pi} \int d(\Delta k) \Phi_t(\Delta k) \frac{\sin\left(\frac{\Delta k_0 - \Delta k}{4}(2z + L)\right)}{\Delta k_0 - \Delta k} e^{i(\Delta k_0 - \Delta k)(2z - L)/4}. \end{aligned} \tag{2.53}$$

Without loss of generality we will consider N odd. We take N odd to simplify the calculations and simplify the way the algorithm works. If instead we choose N to be even we would then need to consider two half domains of length $l_c/2$ at the beginning and end of the crystal.

We now index the crystal every coherence length to implement the algorithm to determine the nonlinearity. In Fig. 2.7 we include a schematic of how the crystal is indexed.

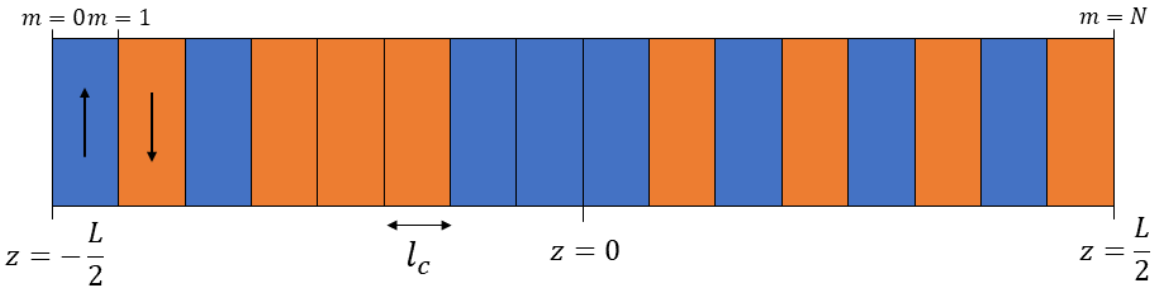

Figure 2.7: Schematic of nonlinear crystal used for calculating the nonlinearity in the algorithm. The crystal extends from $-L/2$ to $L/2$ and is centered at $z = 0$. The crystal is broken up into N pieces each with length l_c such that $L = Nl_c$ and indexed by m. In each domain the nonlinearity is either ± 1, in the above image the nonlinearity for the first three domains is +1,-1. In a real crystal N is typically on the order of $500 - 2000$.

The position along the crystal is given by $z = -L/2 + ml_c$ for some integer m. The nonlinearity every coherence length is determined by looking at whether the function was increasing/decreasing in the previous domain and whether it should increase/decrease in the next domain. We initialize the algorithm by

- if $\sin(N\pi/2) > 0$
  - if $A_t(-L/2 + l_c) > 0$ then $g(0) = +1$
  - if $A_t(-L/2 + l_c) < 0$ then $g(0) = -1$
- if $\sin(N\pi/2) < 0$
  - if $A_t(-L/2 + l_c) > 0$ then $g(0) = -1$
  - if $A_t(-L/2 + l_c) < 0$ then $g(0) = +1$

then for each subsequent domain we calculate the cost function C to determine the poling:

- Calculate $C = A_t(z + l_c) - A_a(z)$
  - if $C > 0$ then the field needs to increase
    - if $A_a(z) > A_a(z - l_c)$ then $g(z) = -g(z - l_c)$, field was increasing flip so it keeps increasing

- if $A_a(z) < A_a(z - l_c)$ then $g(z) = g(z - l_c)$, field was decreasing it will increase in the next domain

- if $C < 0$ then the field needs to decrease
  - if $A_a(z) > A_a(z - l_c)$ then $g(z) = g(z - l_c)$, field was increasing it will decrease in the next domain
  - if $A_a(z) < A_a(z - l_c)$ then $g(z) = -g(z - l_c)$, field was decreasing flip so it keeps decreasing

After the algorithm calculates the nonlinearity profile we can check if its correct by plotting $A_a(z)$ on top of $A_t(z)$ for a continuous range of z values. For each z calculate $m = \lfloor z/l_c + N/2 \rfloor$ then

$$\begin{aligned} &A_a(-L/2 + ml_c \leq z \leq -L/2 + (m+1)l_c) = A_a(-L/2 + ml_c) + \\ &2g_a(-L/2 + ml_c)\frac{\sin(\Delta k_0(z + L/2 - ml_c)/2)}{\Delta k_0} e^{i\Delta k_0(z - L/2 + ml_c)/2}. \end{aligned} \tag{2.54}$$

Finally, we use the approximate form of the nonlinearity $g_a(z)$ determined by the algorithm to calculate the approximate PMF $\Phi_a(\Delta k)$,

$$\begin{aligned} \Phi_a(\Delta k) &= \int_{-L/2}^{L/2} dz g_a(z) e^{i\Delta kz} \\ &= \sum_{n=0}^{N-1} \int_{-L/2+nl_c}^{-L/2+(n+1)l_c} dz g_a(-L/2 + nl_c) e^{i\Delta kz} \\ &= 2\frac{\sin(\Delta kl_c/2)}{\Delta k} e^{i\Delta kl_c(1-N)/2} \sum_{n=0}^{N-1} g_a(-L/2 + nl_c) e^{i\Delta kl_c n}. \end{aligned} \tag{2.55}$$

Taking the real part of the approximate PMF

$$\Re(\Phi_a(\Delta k)) = 2\frac{\sin(\Delta kl_c/2)}{\Delta k} \sum_{n=0}^{N-1} g_a(-L/2 + nl_c) \cos(\Delta k(l_c n + l_c(1-N)/2)), \tag{2.56}$$

we find that $\Re(\Phi_a(\Delta k))$ is symmetric function of Δk. We include an example of tailoring a nonlinear crystal so that the PMF is a Gaussian in Appendix A.

Constraints on the Target Phasematching Function

When engineering a nonlinear crystal there are some constraints as to what the target PMF can be. All nonlinear engineering methods rely on coherently adding sinusoidal waves every coherence length. Target PMF are thus restricted to the slope of sinusoidal curve over the length of its coherence length [35]. For the function $\sin x$, which has a coherence length of π, the average slope over its coherence length is given by $(\sin 3\pi/2 - \sin \pi/2)/\pi = 2/\pi$. Thus the slope of the target amplitude must not be greater than $2/\pi$. If it is, then we cannot design a nonlinear crystal to accurately approximate it. In Eq. (2.48) we defined the amplitude of the PMF throughout the crystal by

$$A_t(\Delta k_0, z) = \int_{-L/2}^{z} dz' g_t(z') e^{i\Delta k_0 z'}, \tag{2.57}$$

then taking the derivative with respect to z we find

$$\frac{dA_t(\Delta k_0, z)}{dz} = g(z) e^{i\Delta k_0 z} \leq \frac{2}{\pi}, \quad \forall z \tag{2.58}$$

to be a valid PMF. For a more detailed example of this restriction see Appendix A

The last constraint has to do with the type of algorithm we are implementing. The algorithm we have outlined above works by tracking the real part of the target amplitude throughout the crystal and flipping the nonlinearity accordingly. Since the real and imaginary part of the amplitude suffer a π phase shift, by flipping the nonlinearity every coherence length the imaginary part of the amplitude is flipped at every node and thus cannot increase but oscillates around zero. We are thus limited to choosing target PMFs that are real. In general, the target PMF can be chosen to also be complex by modifying the algorithm to flip the nonlinearity at fractions of the coherence length as was done in [44]. From this point on we will only be considering real PMFs, as this is what the algorithm we are using allows.

Chapter 3

Encoding Modes as Gaussian Frequency Distributions

In optics, there are various ways to define modes of light. Fundamentally, a mode is a plane wave with wave vector $\mathbf{k}$ and polarization I. Under certain approximations, one can think of $\mathbf{k}$ as a single frequency ω in a spatial mode of an interferometer. One can also define other modes, such as temporal modes (used in, e.g., time-bin encoding of information [45]) or Schmidt modes, which have the benefits of both time-bin encoding and frequency encoding [46].

It is common to decompose the JSA via the Schmidt decomposition, provided in Eq. (2.35). This yields a product of TMSV states, given in Eq. (2.39). These product states are often called multimode squeezed states in the literature, since there are usually many Schmidt modes present for a given JSA. In this thesis, we will refer to these states as Schmidt mode product states because we reserve the term "multimode" to mean something else. Schmidt mode product states have led to advancements in continuous variable quantum information, with the advantage of having more than one mode, one can encode more information in a way that minimizes loss [47]. The downside of Schmidt mode product states for quantum information protocols is that the different modes are hard to distinguish. To distinguish between the different Schmidt modes requires quantum pulsed gates [20], which in practice is experimentally difficult. Here we introduce another encoding in terms of Gaussian frequency distributions. Our modes are only approximately orthogonal but the overlap is negligible. They are localized in time-frequency, which makes them useful for quantum information protocols, and they are easier to distinguish than Schmidt modes. While encoding information into Gaussian frequency distributions is not new, this is the first time it has been discussed in the context of squeezed states.

3.1 Single-Mode Squeezed Vacuum States

Suppose now that we have a JSA that is schematically given by Fig. 3.1 and that the photons all have the same polarization. The JSA in Fig. 3.1 is centered around $(\omega_s, \omega_i) = (\Omega_a, \Omega_a)$. Since the JSA is symmetric and centered around the same center frequency, we can decompose it by the same function. For this example, there is a unique decomposition of the JSA, which is equivalent to the Schmidt decomposition, by Gaussian functions centered at ω_a with a width that matches the JSA. For a normalized Gaussian centered at ω_a defined by $G_a(x)$, we decompose the JSA as

$$\text{JSA}(\omega_i, \omega_s) = \gamma_{aa} G_a(\omega_s) G_a(\omega_i), \tag{3.1}$$

then defining the operators

$$\hat{A}^\dagger = \int d\omega \hat{a}^\dagger(\omega) G_a(\omega), \tag{3.2}$$

the output state (assuming the same polarization) would be given by

$$|\psi\rangle = e^{i\gamma_{aa}\hat{A}^\dagger\hat{A}^\dagger + H.c.} |0\rangle . \tag{3.3}$$

We interpret the operator $\hat{A}^\dagger$ acting on the vacuum as creating a single photon with a frequency distribution given by $G_a(\omega)$. With the above JSA and the decomposition we provided, we generated a SMSV state, where the modes of the field are Gaussian frequency distributions.

One typically has the intuition that JSAs that are elliptical functions correspond to squeezed states. However, in our encoding of the modes as Gaussian frequency distributions, the JSA for a single-mode squeezed states is given schematically by Fig. 3.1. We now show why we call Eq. (3.3) a "squeezed state". We begin by noting the form of Eq. (3.3) is almost identical to to the form of a SMSV state in [23]. We therefore conclude that the squeezing operator has the following transformations on the creation/annihilation operators given by

$$\begin{aligned} \hat{S}^\dagger(\gamma_{aa})\hat{A}\hat{S}(\gamma_{aa}) &= \cosh(2r_{aa})\hat{A} + ie^{i\theta_{aa}}\sinh(2r_{aa})\hat{A}^\dagger \\ \hat{S}^\dagger(\gamma_{aa})\hat{A}^\dagger\hat{S}(\gamma_{aa}) &= \cosh(2r_{aa})\hat{A}^\dagger - ie^{-i\theta_{aa}}\sinh(2r_{aa})\hat{A}, \end{aligned} \tag{3.4}$$

where we set $\gamma_{aa} = r_{aa}e^{i\theta_{aa}}$. We define the quadrature operators $\hat{X}_a$ and $\hat{Y}_a$, which are the generalized position and momentum operators of the field as

$$\begin{aligned} \hat{X}_a &= \frac{1}{\sqrt{2}}(\hat{A} + \hat{A}^\dagger) \\ \hat{Y}_a &= \frac{1}{i\sqrt{2}}(\hat{A} - \hat{A}^\dagger). \end{aligned} \tag{3.5}$$

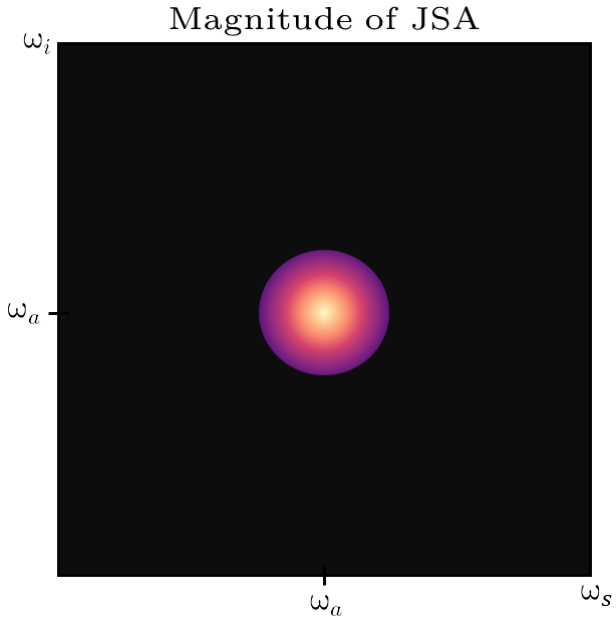

Figure 3.1: Schematic JSA

We now calculate the affect that the squeezing operator has on the quadrature operators to be

$$\begin{aligned} \hat{S}^\dagger(\gamma_{aa})\hat{X}_a\hat{S}(\gamma_{aa}) &= e^{2\theta_{aa}}\hat{X}_a \\ \hat{S}^\dagger(\gamma_{aa})\hat{Y}_a\hat{S}(\gamma_{aa}) &= e^{-2\theta_{aa}}\hat{Y}_a, \end{aligned} \tag{3.6}$$

where we have set $\theta_{aa} = \pi/2$. In Eq. (3.6) we see the affect that the squeezing operator has on the quadrature operators. When plotted in phase space, the squeezing operator deforms the vacuum error into an ellipse [23].

3.2 Two-Single Mode Squeezed Vacuum States

Defining the modes of the field as Gaussian frequency distributions has various benefits, the first being that it is easily generalized to more than two modes. Now, suppose that we have a JSA schematically given in Fig. 3.2. The JSA now has two contributions centered at $(\omega_s, \omega_i) = (\Omega_a, \Omega_a)$ and $(\omega_s, \omega_i) = (\Omega_b, \Omega_b)$. We now apply a similar decomposition as we did for the one-amplitude JSA in Fig. 3.1 and decompose it with Gaussians centered

at ω_a and ω_b as

$$\text{JSA}(\omega_s, \omega_i) = \gamma_{aa} G_a(\omega_s) G_a(\omega_i) + \gamma_{bb} G_b(\omega_s) G_b(\omega_i), \tag{3.7}$$

then we define similar operators given by

$$\begin{aligned} \hat{A}^\dagger &= \int d\omega \hat{a}^\dagger(\omega) G_a(\omega) \\ \hat{B}^\dagger &= \int d\omega \hat{a}^\dagger(\omega) G_b(\omega). \end{aligned} \tag{3.8}$$

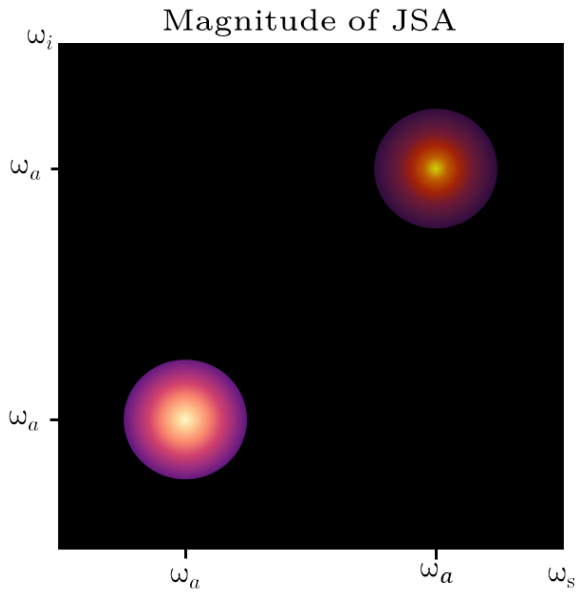

Figure 3.2: Schematic JSA for a state corresponding to two SMSV states. The different colors represent different amplitudes.

For two Gaussians separated by a shift, the overlap between them is given by

$$\begin{aligned} \int dx G(x) G(x \pm \delta x) &= \frac{1}{\sigma\sqrt{\pi}} e^{-\frac{-\delta x^2}{4\sigma^2}} \\ \int dx G(x) G(x \pm \delta x) \Big|_{\delta x = 10\sigma} &= \frac{1}{\sigma} 7.83 \times 10^{-12}, \end{aligned} \tag{3.9}$$

which for our purposes, is negligible. Under this assumption, the operators $\hat{A}^\dagger$ and $\hat{B}^\dagger$ satisfy the following commutation relations

$$\left[\hat{A}, \hat{A}^\dagger\right] = \left[\hat{B}, \hat{B}^\dagger\right] = 1, \quad \left[\hat{A}, \hat{B}\right] = 0, \tag{3.10}$$

which are the same as if the two modes were due to two polarizations or two spatial locations. The state corresponding to the JSA (again assuming the same polarization) is given by

$$|\psi\rangle = e^{i\gamma_{aa}\hat{A}^\dagger\hat{A}^\dagger + i\gamma_{bb}\hat{B}^\dagger\hat{B}^\dagger + H.c.}\,|0\rangle\,. \tag{3.11}$$

Since each mode is orthogonal, in this case we can separate the exponential into a product of single-mode squeezed states given by

$$\begin{aligned} |\psi\rangle &= e^{i\gamma_{aa}\hat{A}^\dagger\hat{A}^\dagger + i\gamma_{bb}\hat{B}^\dagger\hat{B}^\dagger + H.c.}\,|0\rangle \\ &= e^{i\gamma_{aa}\hat{A}^\dagger\hat{A}^\dagger + H.c.}\,|0\rangle \otimes e^{i\gamma_{bb}\hat{B}^\dagger\hat{B}^\dagger + H.c.}\,|0\rangle\,. \end{aligned} \tag{3.12}$$

We have generated a state using Gaussian frequency modes similar to the product state in Eq. (2.39) which was build up of Schmidt modes.

3.3 Two-Mode Squeezed Vacuum States

Next we consider the JSA given by Fig. 3.3. The JSA again has two amplitudes but now located at $(\omega_s, \omega_i) = (\Omega_a, \Omega_b)$ and $(\omega_s, \omega_i) = (\Omega_b, \Omega_a)$. Performing a similar decomposition of the JSA in terms of Gaussians centered at ω_a and ω_b as

$$\text{JSA}(\omega_s, \omega_i) = \gamma_{ab} G_a(\omega_s) G_b(\omega_i) + \gamma_{ba} G_b(\omega_s) G_a(\omega_i) \tag{3.13}$$

where γ_{ab} corresponds to the top left amplitude and γ_{ba} the bottom right amplitude. Using the same definition of the operators $\hat{A}$ and $\hat{B}$, (assuming the same polarization) we can write the output state as

$$|\psi\rangle = e^{i(\gamma_{ab}+\gamma_{ba})\hat{A}^\dagger\hat{B}^\dagger + H.c.}\,|0\rangle\,. \tag{3.14}$$

The state generated in Eq. (3.14) is a TMSV state where each mode is a Gaussian frequency distribution centered at ω_a or ω_b.

3.4 Generalized Modes and Linear-Optical Transformations

In the above sections we showed that we can decompose the JSAs in Fig. 3.1, 3.2 and 3.3 by Gaussian frequency distributions centered at the center frequencies of the JSA. In this section we use the intuition built up in the previous sections to extend the process of encoding modes as Gaussian frequency distributions to many modes and then discuss linear-optical transformations on the modes.

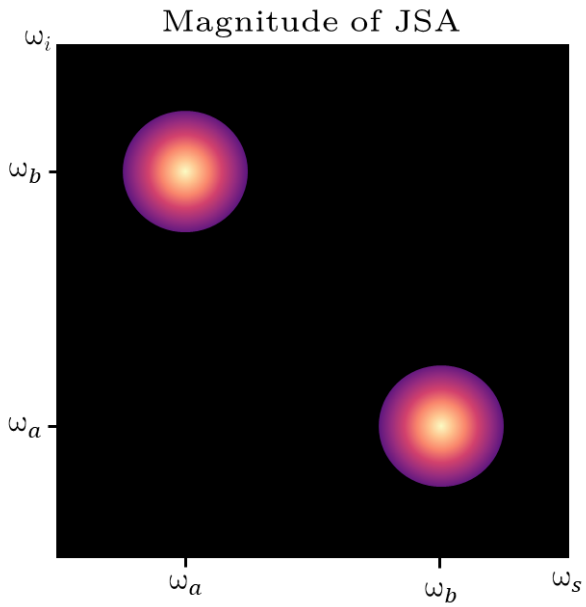

Figure 3.3: Schematic JSA for a state corresponding to a TMSV state.

3.4.1 Extending Gaussian Frequency Distributions to Many Modes

Suppose we have a JSA that has amplitudes at many frequencies denoted by ω_n. We imagine decomposing the JSA in a similar way by Gaussians $G_n(\omega)$ centered at ω_n. We assume each $G_n(\omega)$ is orthogonal to $G_m(\omega)$, for every n, m. We define similar operators for each ω_n as

$$\hat{A}_n^\dagger = \int d\omega G_n(\omega)\hat{a}^\dagger(\omega). \tag{3.15}$$

Which due to the properties of $G_n(\omega)$ satisfy

$$[A_n, A_m^\dagger] = \delta_{nm}, \quad [A_n, A_m] = [A_n^\dagger, A_m^\dagger] = 0. \tag{3.16}$$

3.4.2 Linear-Optical Transformations

In Section 2.2, we discussed linear-optical transformations that included polarizing beam splitters, half wave plates and beam splitters. In this section we apply the three sets of transformations to the generalized operators $\hat{A}_n^\dagger$. The operators $\hat{A}_n^\dagger$ are made up of Gaussian frequency distributions but because each optical transformation is linear and frequency independent we can directly apply them to the operator.

Polarizing Beam Splitters

In Section 2.2.1 we introduced the polarizing beam splitter transformations. The polarizing beam splitter transformations acting on $\hat{A}_n^\dagger$ are given by

$$\begin{aligned}
\hat{U}_{PBS}\hat{A}_{H,n}^{(1)}\hat{U}_{PBS}^\dagger &= \hat{A}_{H,n}^{(1')} \\
\hat{U}_{PBS}\hat{A}_{V,n}^{(1)}\hat{U}_{PBS}^\dagger &= \hat{A}_{V,n}^{(2')} \\
\hat{U}_{PBS}\hat{A}_{H,n}^{(2)}\hat{U}_{PBS}^\dagger &= \hat{A}_{H,n}^{(1')} \\
\hat{U}_{PBS}\hat{A}_{V,n}^{(2)}\hat{U}_{PBS}^\dagger &= \hat{A}_{V,n}^{(2')},
\end{aligned} \tag{3.17}$$

where the superscript (1) and (2) denote the spatial degree of freedom in paths 1 and 2.

Half Wave Plate

Next we consider the half wave plate transformations given in Section 2.2.2. For an angle $\varphi = \pi/4$, the half-wave plate transformations acting on the operators $\hat{A}_{H,n}^\dagger$ is given by

$$\begin{aligned}
\hat{U}_{HWP}(\pi/4)\hat{A}_{H,n}\hat{U}_{HWP}^\dagger(\pi/4) &= \int d\omega G_n(\omega)\hat{U}_{HWP}(\pi/4)\hat{a}_H^\dagger(\omega)\hat{U}_{HWP}^\dagger(\pi/4) \\
&= \int d\omega G_n(\omega) i\hat{a}_V(\omega) \\
&= i\hat{A}_{V,n}.
\end{aligned} \tag{3.18}$$

Beam Splitter

Lastly we calculate the beam splitter transformations in section 2.2.3 with $\theta = 0$, acting on $\hat{A}^{\dagger}_{H,n}$ as

$$\begin{aligned}
\hat{U}^{\dagger}_{BS} A^{\dagger,(1)}_{n} \hat{U}_{BS} &= \int d\omega G_n(\omega) \hat{U}^{\dagger}_{BS} a^{\dagger}_1(\omega) \hat{U}_{BS} \\
&= \frac{1}{\sqrt{2}} \int d\omega G_n(\omega) (a^{\dagger}_1(\omega) + a^{\dagger}_2(\omega)) \\
&= \frac{1}{\sqrt{2}} \left(A^{\dagger,(1)}_{n} + A^{\dagger,(2)}_{n} \right) \\
\hat{U}^{\dagger}_{BS} A^{\dagger,(2)}_{n} \hat{U}_{BS} &= \int d\omega G_n(\omega) \hat{U}^{\dagger}_{BS} a^{\dagger}_2(\omega) \hat{U}_{BS} \\
&= \frac{1}{\sqrt{2}} \int d\omega G_n(\omega) (-a^{\dagger}_1(\omega) + a^{\dagger}_2(\omega)) \\
&= \frac{1}{\sqrt{2}} \left(-A^{\dagger,(1)}_{n} + A^{\dagger,(2)}_{n} \right) .
\end{aligned} \tag{3.19}$$

We have shown how one can generate SMSV states, a product of two SMSV states and TMSV states by the appropriate JSA and decomposing using Gaussian frequency distributions. We then extended this process to an arbitrary number of Gaussians and calculated the linear-optical transformations acting on the operators $\hat{A}^{\dagger}_{n}$. In the next chapter we will propose a method to generate a JSA which will correspond to a hybrid squeezed state.

Chapter 4

Tunable Hybrid Squeezed States of Light

Hybrid approaches combine the best of both worlds. In the field of quantum optics, examples include encoding quantum information into Schmidt modes [48], which combines the benefits of time and frequency encoding, and entangling qubits to qumodes [1] to reap the benefit of both discrete and continuous variables. In this chapter, we introduce, and describe the generation of hybrid squeezed states, which have features of single-mode and two-mode squeezed vacuum states.

We define a hybrid squeezed state as follows:

$$|\{\beta\}\rangle = e^{\frac{\beta_{aa}^*}{2}a^\dagger a^\dagger + \frac{\beta_{ab}^*}{2}a^\dagger b^\dagger + \frac{\beta_{ba}^*}{2}a^\dagger b^\dagger + \frac{\beta_{bb}^*}{2}b^\dagger b^\dagger - H.c}|0\rangle\,. \tag{4.1}$$

By taking the constants $\beta_{aa} = \beta_{bb} = 0$ we recover the TMSV state in Eq. (2.10). Similarly, setting $\beta_{ab} = \beta_{ba} = \beta_{bb} = 0$ recovers the SMSV state in Eq. (2.9). Using the intuition built up in Chaper 3, we propose that the JSA for a state that is both single- and two-mode squeezed would schematically be given by Fig. 4.1. This JSA has four amplitudes located at (ω_a, ω_a), (ω_a, ω_b), (ω_b, ω_a) and (ω_b, ω_b), each corresponding to a squeezing term in Eq. (4.1) for the hybrid squeezed state.

In Chapter 2, we derived that the JSA is given by the multiplication of the pump and the PMF. Due to the energy conservation of a SPDC process, the pump function must strictly be on the anti diagonal. With this restriction, there is no way to generate the JSA shown in Fig. 4.1 by multiplying a diagonal PMF with an anti diagonal pump. Any way

[1] Qumodes are continuous variable generalizations of qubits.

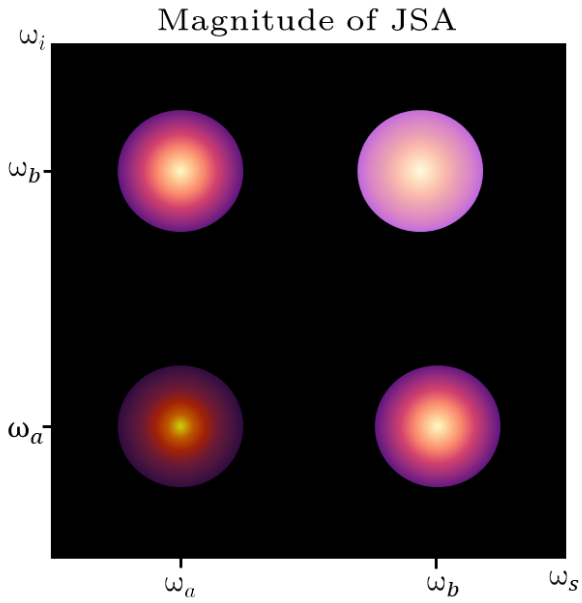

Figure 4.1: Schematic of the JSA corresponding to a state that is both single- and two-mode squeezed. Circles with different shading indicate different peak amplitudes.

of multiplying these two functions will result in a diamond style pattern, e.g. the JSA in Fig. 4.2. To generate the desired JSA we will first create a JSA in a diamond pattern with more than four amplitudes and then "delete" some while leaving the desired peaks.

We begin with a PMF and pump functions that each have three Gaussian function separated by some amount sufficiently large enough that the overlap between them is negligible. Multiplying these two functions together would generate a JSA schematically shown in Fig. 4.2, which has nine amplitudes.

To generate the JSA with four amplitudes in Fig. 4.1 from the JSA in Fig. 4.2 with nine amplitudes we must implement some form of spectral filtering to remove the amplitudes at the locations marked with an X. Alternatively, one could suppress the generation of these peaks by engineering a Bragg grating *into* the nonlinear material to induce a stop band at the frequencies of the undesired peaks [49]. This is much more challenging but has the benefit of removing the peaks coherently. In either case, the JSA with four amplitudes shown in Fig. 4.1 will be left over as desired.

In the next section we describe a method for engineering a pump function that, when combined with an engineered nonlinear crystal, can generate the desired JSA.

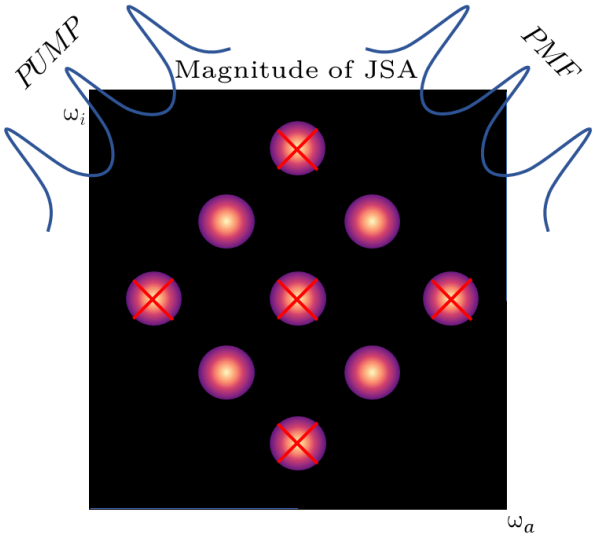

Figure 4.2: Schematic of the JSA that would be produced by multiply a PUMP and PMF each with three Gaussian peaks.

4.1 Pump Pulse Shaping

For the pump function we require three Gaussians that are the same width and separated by the same shift, the desired pump amplitude function is given by

$$\Psi(\omega_p) = b_{-1}G(\omega_p - \Omega_p + \delta\omega_p) + b_0 G(\omega_p - \Omega_p) + b_1 G(\omega_p - \Omega_p - \delta\omega_p), \tag{4.2}$$

where $G(x)$ is define by

$$G(x) = \frac{1}{\sigma\sqrt{2\pi}} e^{-\frac{x^2}{2\sigma^2}}, \tag{4.3}$$

where $\Omega_p = \Omega_s + \Omega_i$ is the center frequency of the downconversion process, $\omega_p = \omega_s + \omega_i$ is set by the energy conservation of the interaction, b_{-1}, b_0, b_1 are the amplitudes of each contribution and $\delta\omega_p$ is the width between each Gaussian. There is a large body of work that has explored how to spectrally engineer a pulse of light with an arbitrary frequency distribution [50]. However, since we require only Gaussian distributions, we propose a mechanism in Fig. 4.3 to combine three Gaussian frequency distributions. The constants b_n can be complex and can be changed in real time, by for, example, removing the blocks in Fig. 4.3. In Fig. 4.4a we plot the pump amplitude as a function of ω_p and in Fig. 4.4b as a function of ω_s, ω_i.

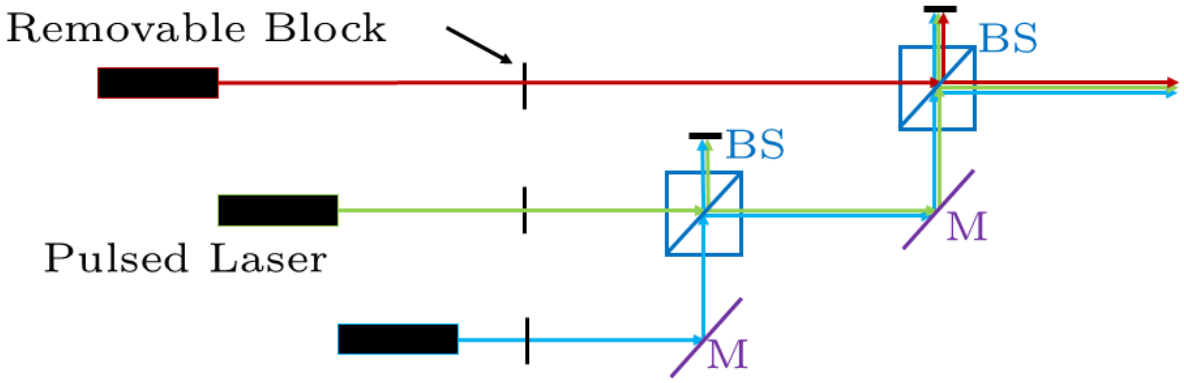

Figure 4.3: Schematic for creating a pump pulse of light that has a frequency distribution of three gaussians. In the figure the colors red, green, blue represent the narrow frequency pulsed light. By removing the block we can change on the fly the input pump light. In the figure BS and M represent a beam splitter and mirror.

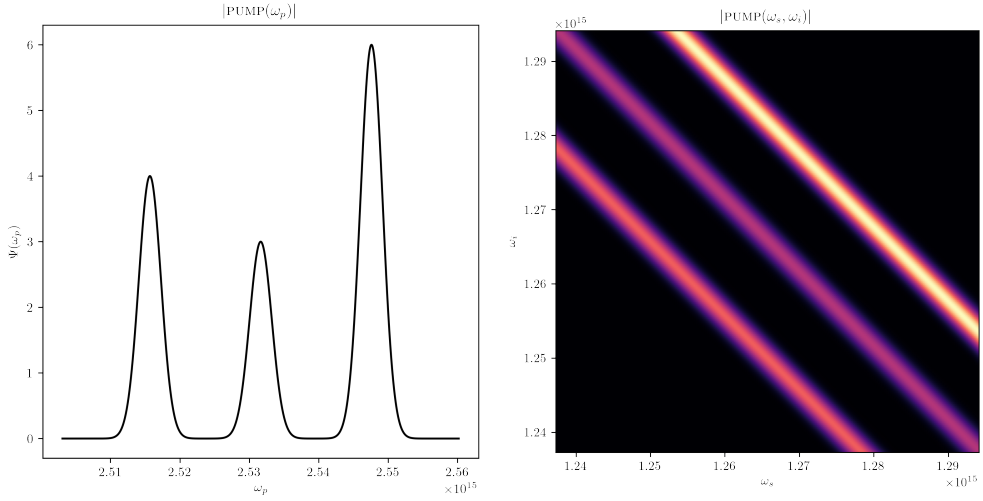

(a) Pump as a function of ω_p

(b) Pump as a function of ω_s, ω_i

Figure 4.4: Pump frequency distribution for three Gaussian's at the same width and separation as the PMF in Fig. 4.6 plotted as a function of ω_p and ω_s, ω_i. The amplitudes coefficients for each peak are $b_{-1} = 4, b_0 = 3, b_1 = 6$.

4.2 Engineering the Phasematching Function

We now design a nonlinear crystal to generate a PMF with three Gaussian peaks, one centered at Δk_0 and the other two centered at $\Delta k_0 \pm \delta k$ using the algorithm described in section 2.5.2. The target PMF is given by

$$\Phi_t(\Delta k) = a_0 G(\Delta k - \Delta k_0 - \delta k) + a_1((G(\Delta k - \Delta k_0 + \delta k) + G(\Delta k - \Delta k_0 - \delta k)) \quad (4.4)$$

where $G(x)$ is defined by Eq. (4.3). From the discussion at the end of section 2.5.2, we take the target PMF to be symmetric by choosing the pre-factor in front of $G(\Delta k - \Delta k_0 + \delta k)$ to be the same as $G(\Delta k - \Delta k_0 - \delta k)$. We take the value $\delta k = 10\sigma$ to ensure the overlap between each Gaussian is negligible.

The constants a_n can, in general, be complex but due to the discussions at the end of Section 2.5.2, the PMF is restricted to being a real function due to the algorithm we are using to design the nonlinear crystal. We thus take the constants a_n to be real. Once we specify a target PMF the constants a_n are fixed. We first specify a target PMF, and calculate the nonlinearity profile that would generate the desired PMF and implement it into a crystal. To change the constants a_n we would need to determine the new nonlinearity profile and redesigning the crystal.

We now use the algorithm discussed in Section 2.5.2 to design a crystal with three Gaussian peaks. All of the crystal properties such as the Sellmeier values, length, phase mismatch and pump/signal/idler frequencies are given in Appendix A. Inputting the target PMF defined in Eq. 4.4 into the algorithm produces a nonlinearity profile shown in Fig. 4.5. In Fig. 4.6 we plot the target and approximate PMF as a function of Δk on the left and the approximate PMF as a function of ω_s, ω_i on the right.

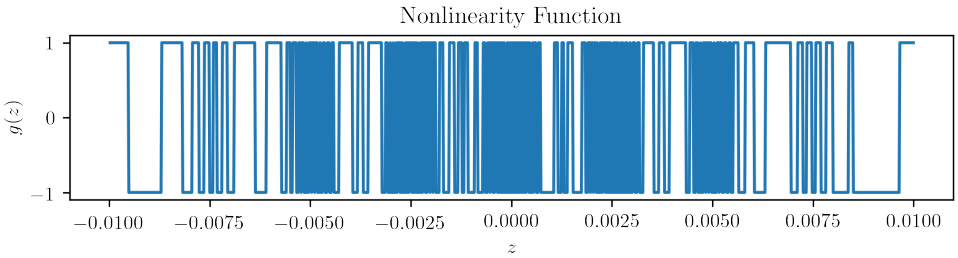

Figure 4.5: Nonlinearity profile for a crystal with the target PMF given by Eq. (4.4).

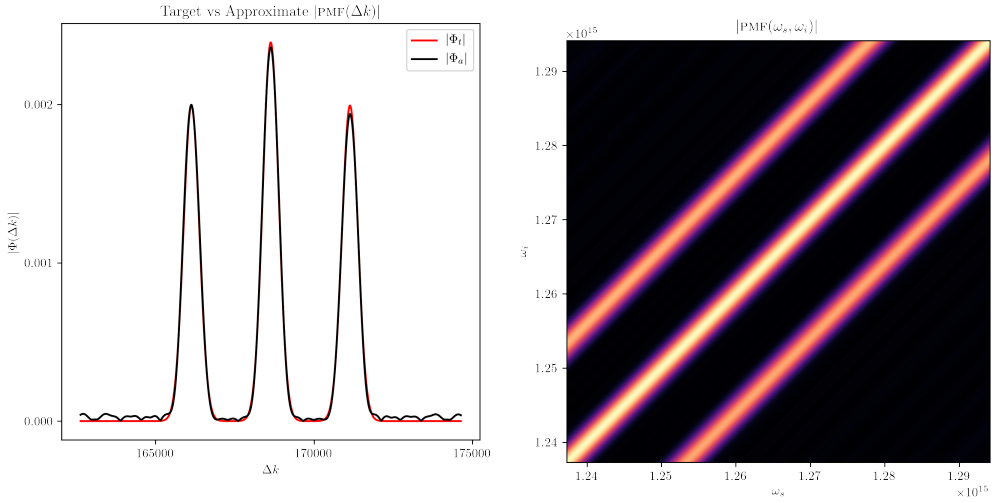

Figure 4.6: PMF as a function of Δk and the signal and idler frequencies for a target PMF given by Eq. (4.4).

4.3 The Joint Spectral Amplitude

In Section 4.1 we proposed a mechanism where we could design the input pump pulse of light to have three Gaussians peaks. We then tailored a nonlinear crystal to generate a PMF given by Eq. (4.4), which has three Gaussian peaks and provided the nonlinearity profile that would produce it in Section 4.2. We chose the width and shifts between the Gaussians to be the same so that the JSA can be decomposed by Gaussians. To calculate the JSA we multiply the PMF in Fig. 4.6 with the pump in Fig. 4.4b together which is shown in Fig. 4.7. We interpret each amplitude of the JSA as the generation of photons at the center signal and idler frequencies. However, since the plot is symmetric there are six unique signal and idler frequencies. When we decompose the JSA, each amplitude will be associated with a squeezing term in the exponential of the output state of the SPDC process in Eq. 2.31. We therefore need to eliminate the frequency generation of five of the amplitudes.

Spectrally Filtering the Joint Spectral Amplitude

By eliminating the horizontal and vertical frequency generation in Fig. 4.7 we would have the desired JSA with four amplitudes. Here we present two methods which could be used to eliminate the unwanted amplitudes.

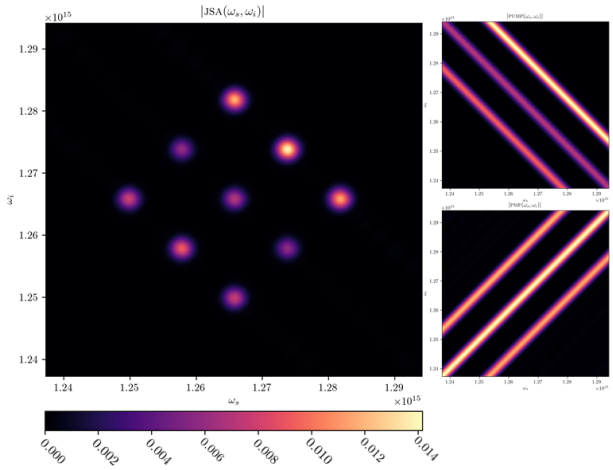

Figure 4.7: JSA, PMF and pump.

The simplest way to eliminate the undesired amplitudes would be to spectrally filter the output state of light. We can implement a spectral filter in two ways. The first is to use a prism to separate out the different modes and then block the undesired ones. The second is to send the output light through a fiber Bragg grating filter. Both of these methods rely on post processing of the state of light.

The second and more ideal method would be to directly engineer the Bragg grating into the nonlinear crystal that is mediating the SPDC process. This would not be a filtering technique but a direct suppression of the generation of light at the frequency of the strips with the X's in Fig. 4.2. Although this has not been accomplished in practice it was theorized in [49].

After filtering, the JSA would be given by Fig. 4.8. We now shift the focus to decomposing the JSA using Gaussian frequency distributions and explicitly show that the JSA we have developed is a hybrid squeezed state.

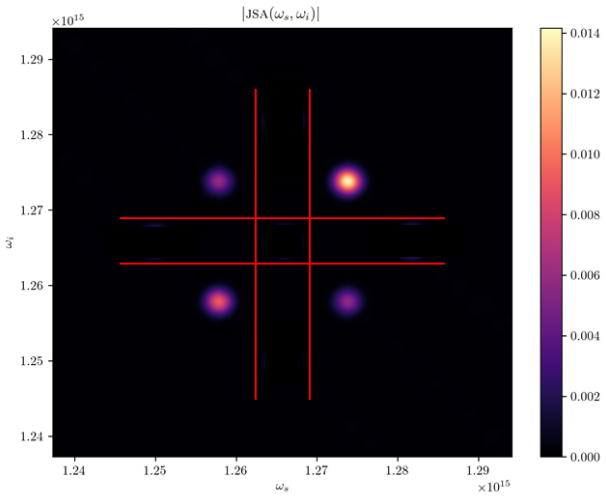

Figure 4.8: JSA after filtering the horizontal and vertical frequency generation

4.4 Providing a Decomposition of the Joint Spectral Amplitude

For amplitudes of the form in Fig. 4.8, we can specify a decomposition similar to the decomposition in Chapter 3. We can decompose the JSA in Fig. 4.8 as

$$\mathrm{JSA}(\omega_s, \omega_i) = \gamma_{aa} G_a(\omega_s) G_a(\omega_i) + \gamma_{ab} G_a(\omega_s) G_b(\omega_i) + \gamma_{ba} G_b(\omega_s) G_a(\omega_i) + \gamma_{bb} G_b(\omega_s) G_b(\omega_i), \tag{4.5}$$

where $G_a(\omega), G_b(\omega)$ were defined in section 3.2. In Eq. (4.5) γ_{aa} corresponds to the lower left amplitude at $(\omega_s, \omega_i) = (\Omega_a, \Omega_a)$, γ_{ab} corresponds to the upper left amplitude at $(\omega_s, \omega_i) = (\Omega_a, \Omega_b)$, γ_{ba} corresponds to the lower right amplitude at$(\omega_s, \omega_i) = (\Omega_b, \Omega_a)$ and γ_{bb} corresponds to the upper right amplitude at $(\omega_s, \omega_i) = (\Omega_b, \Omega_b)$. It is important to note that this decomposition, in general, is not equal to the Schmidt decomposition for the filtered JSA in Fig. 4.8.

Using the definition of the operators $\hat{A}^\dagger$, $\hat{B}^\dagger$ in Eq. (3.8) we write the output state of the SPDC process as

$$|\psi\rangle = \exp\left(i(\gamma_{aa}\hat{A}_H^\dagger \hat{A}_V^\dagger + \gamma_{ab}\hat{A}_H^\dagger \hat{B}_V^\dagger + \gamma_{ba}\hat{B}_H^\dagger \hat{A}_V^\dagger + \gamma_{bb}\hat{B}_H^\dagger \hat{B}_V^\dagger) + H.c.\right)|0\rangle\,. \tag{4.6}$$

Unlike in Chapter 3, where we assumed the same polarization, the operators in Eq. 4.6 have an extra degree of freedom because the output of the SPDC process generates photons

with orthogonal polarization. In Eq. 4.6 the output of the SPDC process is in the form of a hybrid squeezed state, it has the single-mode squeezing terms $\hat{A}^2, \hat{B}^2$ and two-mode squeezing terms $\hat{A}\hat{B}, \hat{B}\hat{A}$. However, this is not the hybrid state that we desire because there is the polarization degree of freedom. To have a real hybrid squeezed state we need to eliminate the polarization degree of freedom which will be the subject of the next section.

4.5 Eliminating the Polarization Degree of Freedom

One way to generate TMSV states is by combining two SMSV states on a beam splitter [15]. We would like to use a similar method, but in reverse, to eliminate the polarization degrees of freedom. We are generating a hybrid squeezed state by interacting a pump pulse with a nonlinear crystal in a 1D wave guide, therefore the photons that come out of the SPDC process are assumed to be in the same spatial degree of freedom. Since the photons are in the same spatial degree of freedom, we can not input them directly onto a beam splitter to separate them.

To eliminate the polarization degree of freedom we will apply a sequence of linear-optical transformations including a polarization beam splitter, half-wave plate and a beam splitter. We begin with a polarization beam splitter after the output of the SPDC process. A polarizing BS will separate the polarization degrees of freedom into two spatial modes. We then apply a half-wave plate to one of the spatial modes which will flip the polarization state to vertical. We now have two pulses of light with the same polarization in different spatial degrees of freedom. We then direct the two pulses onto a beam splitter. A schematic of the set of transformations is shown in Fig. 4.9.

We now apply each transformation to the state in Eq. (4.6), beginning with the polarizing beam splitter,

$$\begin{aligned}\hat{U}_{PBS}\left|\psi\right\rangle &= \hat{U}_{PBS}e^{i(\gamma_{aa}\hat{A}_H^\dagger\hat{A}_V^\dagger+\gamma_{ab}\hat{A}_H^\dagger\hat{B}_V^\dagger+\gamma_{ba}\hat{B}_H^\dagger\hat{A}_V^\dagger+\gamma_{bb}\hat{B}_H^\dagger\hat{B}_V^\dagger)+H.c.}\left|0\right\rangle \\ &= e^{i(\gamma_{aa}\hat{A}_{H,1}^\dagger\hat{A}_{V,2}^\dagger+\gamma_{ab}\hat{A}_{H,1}^\dagger\hat{B}_{V,2}^\dagger+\gamma_{ba}\hat{B}_{H,1}^\dagger\hat{A}_{V,2}^\dagger+\gamma_{bb}\hat{B}_{H,1}^\dagger\hat{B}_{V,2}^\dagger)+H.c.}\left|0\right\rangle,\end{aligned} \tag{4.7}$$

where the subscripts denote the horizontally polarized light in path 1 and vertically polarized light in path 2. Next we apply a half-wave plate to the state and use the set of transformations given in section 3.4.2 for $n = a, b$,

$$\begin{aligned}\hat{U}_{HWP}\hat{U}_{PBS}\left|\psi\right\rangle &= \hat{U}_{HWP}e^{i(\gamma_{aa}\hat{A}_{H,1}^\dagger\hat{A}_{V,2}^\dagger+\gamma_{ab}\hat{A}_{H,1}^\dagger\hat{B}_{V,2}^\dagger+\gamma_{ba}\hat{B}_{H,1}^\dagger\hat{A}_{V,2}^\dagger+\gamma_{bb}\hat{B}_{H,1}^\dagger\hat{B}_{V,2}^\dagger)+H.c.}\left|0\right\rangle \\ &= e^{i(\gamma_{aa}i\hat{A}_{V,1}^\dagger\hat{A}_{V,2}^\dagger+\gamma_{ab}i\hat{A}_{V,1}^\dagger\hat{B}_{V,2}^\dagger+\gamma_{ba}i\hat{B}_{V,1}^\dagger\hat{A}_{V,2}^\dagger+\gamma_{bb}i\hat{B}_{V,1}^\dagger\hat{B}_{V,2}^\dagger)+H.c.}\left|0\right\rangle \\ &= e^{-(\gamma_{aa}\hat{A}_1^\dagger\hat{A}_2^\dagger+\gamma_{ab}\hat{A}_1^\dagger\hat{B}_2^\dagger+\gamma_{ba}\hat{B}_1^\dagger\hat{A}_2^\dagger+\gamma_{bb}\hat{B}_1^\dagger\hat{B}_2^\dagger)+H.c.}\left|0\right\rangle,\end{aligned} \tag{4.8}$$

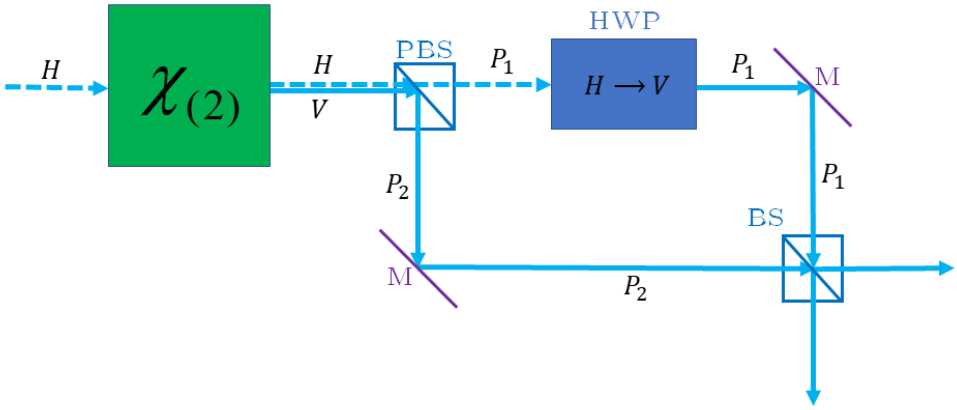

Figure 4.9: Set of transformation to eliminate the polarization degree of freedom. The line style represents the polarization of light. P_1 and P_2 represent the spatial degrees of freedom, PBS is a polarizing beam splitter, HWP is a half wave plate, BS is a beam beam splitter and M is a mirror. Dashed and solid lines represent H and V polarization respectively.

where we have dropped the polarization degree of freedom since now all modes are the same polarization. Next we apply a beam splitter to the state but first calculate the effect that the BS transformation has on each term of the exponential. Using the transformation in section 3.4.2 we find

$$\hat{A}_1^\dagger \hat{A}_2^\dagger \to \frac{-1}{2}\left(\hat{A}_1^\dagger \hat{A}_1^\dagger - \hat{A}_2^\dagger \hat{A}_2^\dagger\right), \tag{4.9}$$

$$\hat{B}_1^\dagger \hat{B}_2^\dagger \to \frac{-1}{2}\left(\hat{B}_1^\dagger \hat{B}_1^\dagger - \hat{B}_2^\dagger \hat{B}_2^\dagger\right), \tag{4.10}$$

$$\hat{A}_1^\dagger \hat{B}_2^\dagger \to \frac{-1}{2}\left(\hat{A}_1^\dagger \hat{B}_1^\dagger - \hat{A}_1^\dagger \hat{B}_2^\dagger + \hat{A}_2^\dagger \hat{B}_1^\dagger - \hat{A}_2^\dagger \hat{B}_2^\dagger\right), \tag{4.11}$$

$$\hat{A}_2^\dagger \hat{B}_1^\dagger \to \frac{-1}{2}\left(\hat{A}_1^\dagger \hat{B}_1^\dagger + \hat{A}_1^\dagger \hat{B}_2^\dagger - \hat{A}_2^\dagger \hat{B}_1^\dagger - \hat{A}_2^\dagger \hat{B}_2^\dagger\right). \tag{4.12}$$

Then acting the BS transformations onto the state

$$
\begin{aligned}
&\hat{U}_{BS}\hat{U}_{HWP}\hat{U}_{PBS}\left|\psi\right\rangle \\
&=\hat{U}_{BS}e^{-(\gamma_{aa}\hat{A}_1^\dagger\hat{A}_2^\dagger+\gamma_{ab}\hat{A}_1^\dagger\hat{B}_2^\dagger+\gamma_{ba}\hat{B}_1^\dagger\hat{A}_2^\dagger+\gamma_{bb}\hat{B}_1^\dagger\hat{B}_2^\dagger)+H.c.}\left|0\right\rangle \\
&=\exp\left(\frac{\gamma_{aa}}{2}\left(\hat{A}_1^\dagger\hat{A}_1^\dagger-\hat{A}_2^\dagger\hat{A}_2^\dagger\right)+\frac{\gamma_{ab}}{2}\left(\hat{A}_1^\dagger\hat{B}_1^\dagger-\hat{A}_1^\dagger\hat{B}_2^\dagger+\hat{A}_2^\dagger\hat{B}_1^\dagger-\hat{A}_2^\dagger\hat{B}_2^\dagger\right)\right. \\
&\left.+\frac{\gamma_{ba}}{2}\left(\hat{A}_1^\dagger\hat{B}_1^\dagger+\hat{A}_1^\dagger\hat{B}_2^\dagger-\hat{A}_2^\dagger\hat{B}_1^\dagger-\hat{A}_2^\dagger\hat{B}_2^\dagger\right)+\frac{\gamma_{bb}}{2}\left(\hat{B}_1^\dagger\hat{B}_1^\dagger-\hat{B}_2^\dagger\hat{B}_2^\dagger\right)-H.c.\right)\left|0\right\rangle \\
&=\exp\left(\frac{\gamma_{aa}}{2}\hat{A}_1^\dagger\hat{A}_1^\dagger+\frac{1}{2}(\gamma_{ab}+\gamma_{ba})\hat{A}_1^\dagger\hat{B}_1^\dagger+\frac{\gamma_{bb}}{2}\hat{B}_1^\dagger\hat{B}_1^\dagger\right. \\
&\left.-(\frac{\gamma_{aa}}{2}\hat{A}_2^\dagger\hat{A}_2^\dagger+\frac{1}{2}(\gamma_{ab}+\gamma_{ba})\hat{A}_2^\dagger\hat{B}_2^\dagger+\frac{\gamma_{bb}}{2}\hat{B}_2^\dagger\hat{B}_2^\dagger)+\frac{1}{2}(\gamma_{ab}-\gamma_{ba})(\hat{A}_2^\dagger\hat{B}_1^\dagger-\hat{A}_1^\dagger\hat{B}_2^\dagger)-H.c.\right)\left|0\right\rangle ,
\end{aligned}
\tag{4.13}
$$

we can eliminate the entangled spatial modes by setting the parameters $\gamma_{ab}=\gamma_{ba}$. If we multiply the two equations for the PMF in Eq. (4.4) and the pump in Eq. (4.2) we find equalities between the parameters $a_0, a_1, b_{-1}, b_0, b_1$ and $\gamma_{aa}, \gamma_{ba}, \gamma_{ab}, \gamma_{bb}$. Comparing terms we find

$$
\gamma_{aa}=b_1a_0,\quad \gamma_{ab}=b_0a_1,\quad \gamma_{ba}=b_0a_1,\quad \gamma_{bb}=b_{-1}a_0, \tag{4.14}
$$

the condition that $\gamma_{ab}=\gamma_{ba}$ is already satisfied due to the symmetric form of Eq. (4.4). Finally, the state after the set of transformation in Fig. 4.9 is

$$
\begin{aligned}
\left|\psi'\right\rangle =&\exp\left(\frac{\gamma_{aa}}{2}\hat{A}_1^\dagger\hat{A}_1^\dagger+\frac{1}{2}(\gamma_{ab}+\gamma_{ba})\hat{A}_1^\dagger\hat{B}_1^\dagger+\frac{\gamma_{bb}}{2}\hat{B}_1^\dagger\hat{B}_1^\dagger-H.c.\right)\left|0\right\rangle\otimes \\
&\exp\left(\frac{-\gamma_{aa}}{2}\hat{A}_2^\dagger\hat{A}_2^\dagger-\frac{1}{2}(\gamma_{ab}+\gamma_{ba})\hat{A}_2^\dagger\hat{B}_2^\dagger-\frac{\gamma_{bb}}{2}\hat{B}_2^\dagger\hat{B}_2^\dagger+H.c.\right)\left|0\right\rangle .
\end{aligned}
\tag{4.15}
$$

The state after the set of linear-optical transformation is two copies of the same state in each spatial mode, where one has a π phase shift. The states are both hybrid squeezed states in the Gaussian frequency modes $\hat{A}$ and $\hat{B}$. In Eq. (4.14) every squeezing amplitude can be varied independently by varying the parameters b_{-1}, b_0, b_1. By changing the pump in real time we can change the value of b_{-1}, b_0, b_1 and tune the state. We have thus successfully generated a tuneable hybrid squeezed state and as an extra get two copies of the state.

Our method of generating tuneable hybrid squeezed states relies on being able to add Gaussian distributions to the PMF and pump amplitude function and applying a set of linear optical transformations. A natural extension to design pump amplitude functions and PMFs with many modes to generate miltimode squeezed states of light.

Chapter 5

Multimode Squeezed Vacuum States

Multimode squeezed states are continuous variable N-partite entangled states which generalize various quantum information protocols [51, 52]. The generation of multimode squeezed states was first proposed in 1999 by P. van Loock and Samuel L. Braunstein [16] which built on top of the technique of [53]. This first method used a sequence of N beam splitters to distribute a single SMSV state to N parties. This method is cumbersome because with many optical elements it becomes harder to stabilize interferometers [54]. This method also relied on entanglement within the spatial modes of the field.

A new method was proposed in [17], which used an optical parametric oscillator and a single periodically poled ferroelectric crystal to generate N mode entangled states. This method is very compact but was limited to four modes. This method was expanded in [18] and lead to the generation of multimode squeezed states with more than four modes. However, both of these methods rely on continuous-wave sources to pump the optical parametric oscillator. A continuous-wave source is not ideal for quantum information protocols, for which we would prefer pulsed sources. Pulsed sources are localized in frequency and time and unbounded, allowing for high dimensional encoding that are compatible with waveguides and fiber transmission [19].

Using the method we developed in Chapter 4 and extending it so that the pump and PMF have many Gaussians we can generate multimode squeezed states. We would like to create a source that is localized in time-frequency and can be used to generate a variety of modes. We now assume we have a JSA generated from a pump and PMF with any number of Gaussians and show that the output is a multimode squeezed state. In Section 5.4 we plot examples of JSAs generated via the algorithm outlined in Section 2.5.2.

5.1 Generalizing the Joint Spectral Amplitude

We begin by assuming we can generate a PMF with any number of Gaussians, with the first centered at Δk_0 and the rest shifted to the left and right by multiples of δk. At the end of Section 6.1.1, we discussed that the approximate PMF is a symmetric function and thus the target PMF must also be symmetric. The target PMF is given by

$$\Phi_t(\Delta k) = \sum_{n=-N}^{n=N} a_n G(\Delta k - \Delta k_0 - n\delta k), \quad a_n = a_{-n}, \tag{5.1}$$

for some set of constants a_n. Also assuming we can generate a pump amplitude function with any number of Gaussians given by

$$\Psi(\omega_p) = \sum_{n=-N}^{n=N} b_n G(\omega_p - \Omega_p + n\delta\omega), \tag{5.2}$$

for some set of constants b_n.

When we multiply the PMF and pump together, the JSA will schematically be given by Fig. 5.1, where we have coloured each amplitude the same for simplicity. For the PMF and pump each having $N_G = 2N + 1$ Gaussians the JSA has N_G^2 amplitudes, however, because we set the PMF to be symmetric there are $M = N_G(N_G+1)/2$ unique amplitudes, and thus M modes.

5.2 Decomposing the Multimode Joint Spectral Amplitude

In Section 4.4 we decomposed the JSA in terms of Gaussian functions centered at Ω_a and Ω_b. Here, we decompose the general multimode JSA in the same way where $G_m(\omega)$ is a Gaussian centered at Ω_m as

$$\text{JSA}(\omega_s, \omega_i) = \sum_{n,m} \gamma_{nm} G_n(\omega_s) G_m(\omega_i), \tag{5.3}$$

where

$$\gamma_{nm} = a_{-\frac{1}{2}(n-m)} b_{-\frac{1}{2}(n+m)}, \tag{5.4}$$

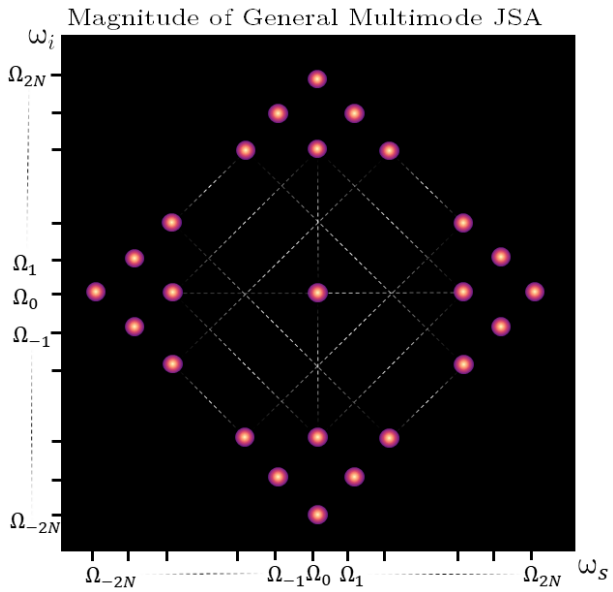

Figure 5.1: Schmatic JSA for a PMF and PUMP made up of $2N+1$ Gaussian. Each amplitude is centered at the frequency $\Omega_{-2N}, .., \Omega_0, ..., \Omega_{2N}$. For simplicity we keep the colour of each amplitude the same.

and the sum is carried out over the restriction that

$$n - m = 0, \pm 2, \pm 4, ..., \pm(2N-2), \pm 2N, \tag{5.5}$$

and the Gaussian functions $G_n(\omega)$ satisfy

$$\int G_n(\omega) G_m(\omega_) \approx \delta_{nm}. \tag{5.6}$$

Swapping the indices for γ_{nm} we find

$$\gamma_{nm} = a_{-\frac{1}{2}(n-m)} b_{-\frac{1}{2}(n+m)} = \gamma_{mn}, \tag{5.7}$$

where we used the property $a_n = a_{-n}$, thus the γ's are symmetric.

Inputting the JSA in Eq. (5.3) and the definition for $\hat{A}_n^\dagger$ in Eq. (3.15) into Eq. (2.31)

we find

$$\begin{aligned}|\psi\rangle &= \exp\left(i\int d\omega_i d\omega_s \mathrm{JSA}(\omega_s,\omega_i)\hat{a}_H^\dagger(\omega_i)\hat{a}_V^\dagger(\omega_s)+H.c.\right)|0\rangle \\ &= \exp\left(i\int d\omega_i d\omega_s \sum_{n,m}\gamma_{nm}G_n(\omega_s)G_m(\omega_i)\hat{a}_H^\dagger(\omega_i)\hat{a}_V^\dagger(\omega_s)+H.c.\right)|0\rangle \\ &= \exp\left(i\sum_{n,m}\gamma_{nm}\hat{A}_{n,H}^\dagger\hat{A}_{m,V}^\dagger+H.c.\right)|0\rangle\,.\end{aligned} \tag{5.8}$$

5.3 Eliminating the Polarization Degree of Freedom for the Multimode State

In Eq. (5.8) we decomposed the JSA into a set of frequency modes with a frequency distribution given by $G_n(\omega)$. However, similar to the hybrid squeezed state, there is still the polarization degree of freedom. To eliminate the polarization degree of freedom we apply the set of transformation in Fig. 4.9. We begin by applying the polarization beam splitter to the state and label the position degree of freedom in the superscript

$$\hat{U}_{PBS}|\psi\rangle = \exp\left(i\sum_{n,m}\gamma_{nm}\hat{A}_{n,H}^{\dagger,(1)}\hat{A}_{m,V}^{\dagger,(2)}+H.c.\right)|0\rangle\,. \tag{5.9}$$

Next we apply the half-wave plate to the state using the transformation in section 3.4.2

$$\begin{aligned}\hat{U}_{HWP}\hat{U}_{PBS}|\psi\rangle &= \exp\left(i\sum_{n,m}\gamma_{nm}i\hat{A}_{n,V}^{\dagger,(1)}\hat{A}_{m,V}^{\dagger,(2)}+H.c.\right)|0\rangle \\ &= \exp\left(-\sum_{n,m}\gamma_{nm}\hat{A}_{n}^{\dagger,(1)}\hat{A}_{m}^{\dagger,(2)}+H.c.\right)|0\rangle\,,\end{aligned} \tag{5.10}$$

where we drop the polarization degree of freedom to simplify the notation. Now we need to eliminate the spatial degree of freedom by sending both spatial modes to the input of a beam splitter. Applying the beam splitter transformations in section 3.4.2, the term in the exponential is transformed by

$$A_n^{\dagger,(1)}A_m^{\dagger,(2)} \to \frac{1}{2}\left(-A_n^{\dagger,(1)}A_m^{\dagger,(1)}+A_n^{\dagger,(1)}A_m^{\dagger,(2)}-A_n^{\dagger,(2)}A_m^{\dagger,(2)}+A_n^{\dagger,(2)}A_m^{\dagger,(2)}\right). \tag{5.11}$$

Putting it all together

$$\begin{aligned}|\psi'\rangle &= \hat{U}_{BS}\hat{U}_{HWP}\hat{U}_{PBS}\,|\psi\rangle \\ &= \exp\left(\frac{1}{2}\sum_{n,m}\gamma_{nm}\left(A_n^{\dagger,(1)}A_m^{\dagger,(1)} - A_n^{\dagger,(1)}A_m^{\dagger,(2)} + A_n^{\dagger,(2)}A_m^{\dagger,(1)} - A_n^{\dagger,(2)}A_m^{\dagger,(2)}\right) - H.c.\right)|0\rangle\,,\end{aligned} \tag{5.12}$$

after exchanging indices on the second term and using the property that $\gamma_{nm} = \gamma_{mn}$ to eliminate the spatial degree of freedom we find

$$\begin{aligned}|\psi'\rangle &= \exp\left(\frac{1}{2}\sum_{n,m}\gamma_{nm}\left(A_n^{\dagger,(1)}A_m^{\dagger,(1)} - A_n^{\dagger,(2)}A_m^{\dagger,(2)}\right) - H.c.\right)|0\rangle \\ &= \exp\left(\frac{1}{2}\sum_{n,m}\gamma_{nm}A_n^{\dagger,(1)}A_m^{\dagger,(1)} - H.c.\right)|0\rangle \otimes \exp\left(-\frac{1}{2}\sum_{n,m}\gamma_{nm}A_n^{\dagger,(2)}A_m^{\dagger,(2)} + H.c.\right)|0\rangle\,.\end{aligned} \tag{5.13}$$

The final state is two copies of a multimode squeezed state with M modes, where the sum is over $n, m = [-2N, 2N]$ such that

$$n - m = 0, \pm 2, \pm 4, ..., \pm(2N-2), \pm 2N. \tag{5.14}$$

Unlike in the two mode case where we had full tunability over each $\gamma_{ab}, \gamma_{aa}, \gamma_{bb}$, in the multmode case we loose some of the tunability. This is clear from Fig. 5.1, we see that each diagonal from the pump multiplies all the PMF amplitudes, thus we cannot increase, for example, the bottom center amplitude without increasing every amplitude along that pump diagonal.

5.4 Generating the Joint Spectral Amplitude for Multimode Squeezed States

We now plot various JSAs that correspond to multimode squeezed states in Fig. 5.2. The plots were made using the nonlinearity shaping algorithm discussed in Section 2.5.2, with various number of peaks ($N_G = 5, 7, 9, 17$) for the pump and PMF. The JSAs plotted correspond to multimode squeezed states defined in Eq. (5.13) with $M = 6, 15, 28, 45, 153$ modes.

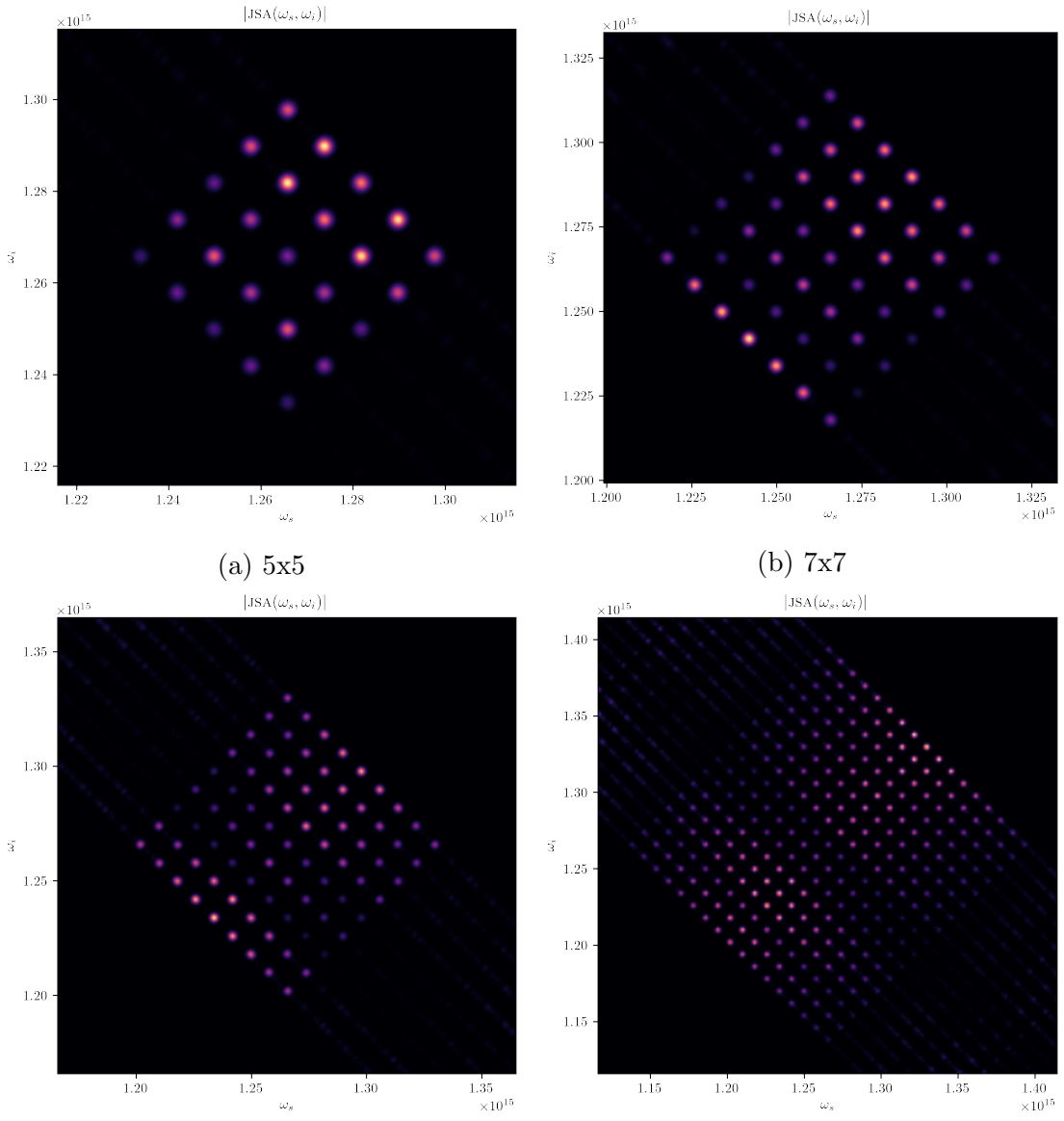

(a) 5x5

(b) 7x7

(c) 9x9

(d) 17x17

Figure 5.2: multimode JSA

In this chapter we proposed a method to generate multimode squeezed states by custom-engineering a nonlinear crystal and pump amplitude function. We can generate multimode squeezed states with many or few modes with a single PMF by changing the pump ampli-

tude coefficients in real time. Our method uses pulsed sources and the modes are Gaussian frequency distributions making them ideal for many quantum information protocols.

Chapter 6

Design Considerations and Fabrication Errors

We beging with design considerations of nonlinear crystals by examining the constraints on the properties of the target PMF and determine optimal parameters for the amplitude coefficients of the PMF, width of the PMF and the number of domains. Next we consider sources of error due to the choice of the target PMF. When designing a nonlinear crystal via ferroelectric poling which was discussed in Section 2.4.4 there are unavoidable set of errors which we simulate and discuss.

6.1 Constraints on the Target Phasematching Function

In this section we consider the constraints on the target PMF, such as the amplitude coefficients, the width of each Gaussian and shape of it. Next we consider a source of error due to oscillations in the target amplitude and show that this error can be reduced by finding the optimal number of domains.

6.1.1 Shape of Target Phasematching function

The first constraint has to do with the shape of the target PMF and whether it is symmetric or not. In Eq. (2.55) we calculated that the real part of the approximated PMF is

symmetric about Δk. Any target PMF must also then be symmetric, if we are going to accurately approximate it from a sum of symmetric functions.

6.1.2 Constraints on the Amplitude coefficients of the Target Phasematching Function

In Section 2.5.2, we showed that the slope of the target PMF must not exceed $2/\pi$ or else we cannot accurately approximate it with a custom poled nonlinear crystal. We now consider what constraints this puts on the amplitude coefficients for the PMF in Eq. (5.1) for the general PMF. We start by calculating the target nonlinearity profile using the inverse Fourier transform as

$$\begin{aligned} g_t(z) &= \frac{1}{2\pi}\int d(\Delta k)\Phi_t(\Delta k)e^{-i\Delta k z} \\ &= \frac{1}{2\pi}\left(a_0 + \sum_{n=1}^{n=N} a_n(e^{in\delta k z} + e^{-in\delta k z})\right)e^{-i\Delta k_0 z}\int d(\Delta k)G(\Delta k)e^{-i\Delta k z} \\ &= \frac{1}{2\pi}e^{-z^2\sigma^2/2}\left(a_0 + 2\sum_{n=1}^{n=N} a_n\cos(n\delta k z)\right)e^{-i\Delta k_0 z}. \end{aligned} \tag{6.1}$$

Then the target amplitude function is

$$\begin{aligned} A_t(z) &= \int_{-L/2}^{z} dz' g_t(z')e^{i\Delta k_0 z'} \\ &= \frac{1}{2\pi}\int_{-L/2}^{z} dz' e^{-z'^2\sigma^2/2}\left(a_0 + 2\sum_{n=1}^{n=N} a_n\cos(n\delta k z')\right), \end{aligned} \tag{6.2}$$

but we are only interested in the slope of the amplitude, so differentiating with respect to z,

$$\frac{dA_t(z)}{dz} = \frac{1}{2\pi}e^{-z^2\sigma^2/2}\left(a_0 + 2\sum_{n=1}^{n=N} a_n\cos(n\delta k z)\right), \tag{6.3}$$

has a maximum when $z = 0$. The slope of the amplitude cannot exceed $2/\pi$, taking the slope at the maximum, we find the constants a_n must satisfy

$$\begin{aligned} \left.\frac{dA_t(z)}{dz}\right|_{z=0} = \frac{1}{2\pi}(a_0 + 2\sum_{n=1}^{n=N} a_n) &\leq \frac{2}{\pi} \\ a_0 + 2(a_1 + a_2 + ... + a_N) &\leq 4. \end{aligned} \tag{6.4}$$

Therefore, as we increase the number of Gaussian functions we must make the constants a_n smaller to ensure that $a_0 + 2(a_1 + a_2 + ... + a_N) \leq 4$. Although we need to decrease the amplitude of the PMF when we increase the number of modes, we can compensate by increasing the pump amplitude, the b_n's.

6.1.3 Optimal Width of the Target Phasematching Function

We now determine the optimal width of each Gaussian given a crystal of length L. For a target PMF with a single Gaussian the target amplitude is the error function. In Fig. 6.1 we plot the target amplitude for different values of the width, $\sigma_{PMF} = 5/L, 6/L, 7/L$. We find that by increasing the width of the Gaussian target PMF the error function "tails" increase. In the "tail" regions the target amplitude is constant, leading the nonlinearity profile being constant over the same region. For the choice of $\sigma_{PMF} = 6/L, 7/L$ we are not using the crystal to its full potential because the end there are regions where the nonlinearity profile is constant. On the other hand, if we cut off the tails prematurely, we get undesired ripples in our PMF.

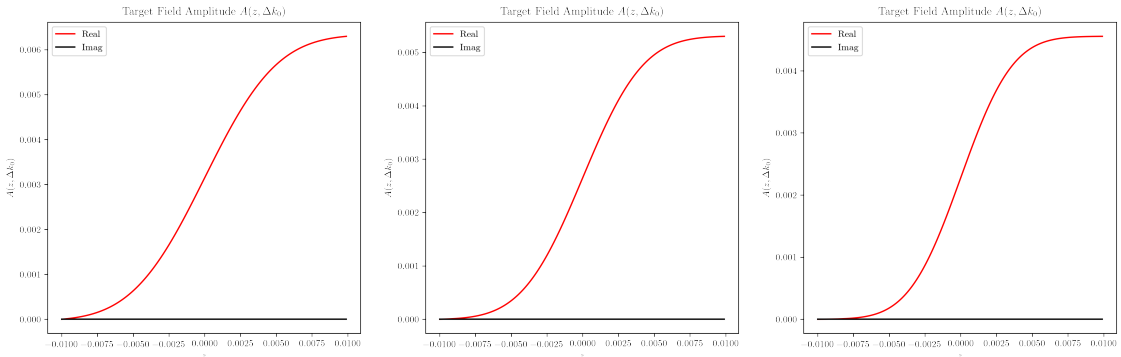

(a) $\sigma = 5/L$ (b) $\sigma = 6/L$ (c) $\sigma = 7/L$

Figure 6.1: Plotting the target amplitude for a Gaussian target PMF for different widths.

For the target PMFs we are interested in they will all be of the form of Eq. (5.1) which has many Gaussians displaced by some fixed amount. One might think that to increase the number of target Gaussians in the PMF one would need a longer crystal but due to the property of Fourier transforms this is not the case. When we take the Fourier transform of a function with a shift we get the Fourier transform of the original function with a phase factor, this can be seen in Eq. (6.2) for the target amplitude for the general PMF in Eq. (5.1). In Eq. (6.2) we see that the target amplitude is the integral of an exponential

(leading to an ampltide that has an error function form) with oscillating terms due to the shifted parts. Thus by adding Gaussians to the PMF the target amplitude shape remains an error function but with oscillations. Now plotting the amplitude for a PMF with five Gaussian peaks and $\sigma_{PMF} = 4/L, 5/L, 6/L$ in Fig. 6.2 we determine that the optimal value of the width of each Gaussian is $\sigma_{PMF} = 5/L$. Thus we have determined the width of each Gaussian and also showed that the number of Gaussians in the PMF is not limited by the length of the crystal.

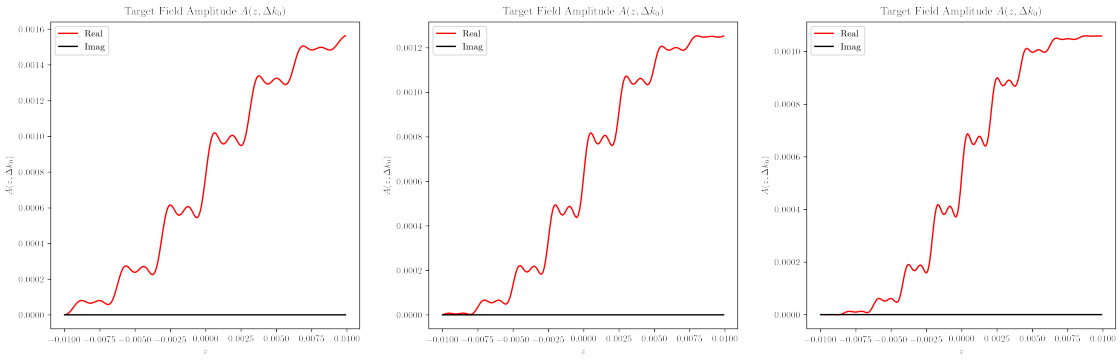

(a) $\sigma = 4/L$ (b) $\sigma = 5/L$ (c) $\sigma = 6/L$

Figure 6.2: Plotting the target amplitude for a five peak Gaussian target PMF.

6.1.4 Sources of Error due to Oscillations of the Target Amplitude

In section 6.1.3 we detailed that for the PMFs we are interested in, the target amplitude will have oscillations. These oscillations can be sources of error when approximating the target PMF if the domain width is on the order of magnitude of the period of oscillation. To approximate a PMF we track the amplitude by coherently adding or subtracting $\sin(\Delta k_0 z)/\Delta k_0$ waves. The approximation has errors when the oscillations of the tracking amplitude are greater than the target amplitude. This is most easily seen in Fig. 6.3 where we show the target amplitude and tracking amplitude for a target PMF with five Gaussians. We see that in the zoomed in region the tracking amplitude oscillations are larger than the target. This is a source of error because in this region the nonlinearity function is set to being constant when there are finer details.

The first solution to this source of error is to choose the constants a_n to be as large as possible given the restriction that $a_0 + 2(a_1 + a_2 + ... + a_N) = 4$. This will increase the

amplitude of the target oscillations to be as large as possible. This solution has a limited benefit. For a PMF with many Gaussians, even setting the constants a_n to the max will not fix the errors. To increase the accuracy of the approximation one needs to consider a finer "resolution" to what we can track. One way to do this would be to introduce sub-coherence length domain engineering, which was proposed by [44]. This is outside of the scope of this thesis since it would require further modification of the algorithm. To simulate sub-coherence domain engineering we instead vary the number of domains while keeping the length fixed.

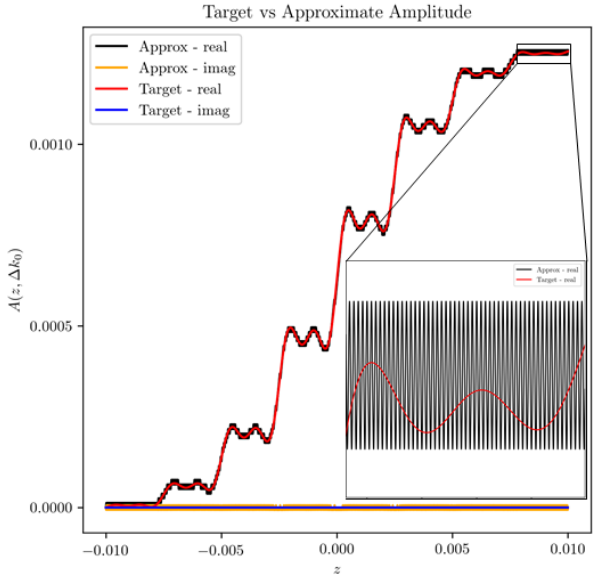

Figure 6.3: Target vs approximate amplitude for a target PMF with five Gaussian peaks. In the zoomed in plot we see how the tracking amplitude cannot accurately approximate the target due the oscillations being too large.

6.1.5 Varying the Number of Domains

In this section we vary the domains while keeping the length of the crystal fixed to determine the optimal number of domains. The length of the crystal is given by $L = Nl_c$, where N is the number of domains and l_c is the coherence length and the length of each domain. If we increase the number of domains we must also decrease the length of each domain to keep the length of the crystal fixed. To determine the optimal number of domains, we

will run the algorithm in section 2.5 for $N = 500, 1000, 1500, 2000, 4000, 6000$ domains. We first take the target PMF to be three Gaussian peaks and plot the target vs approximate PMF for different values of N in Fig. 6.4.

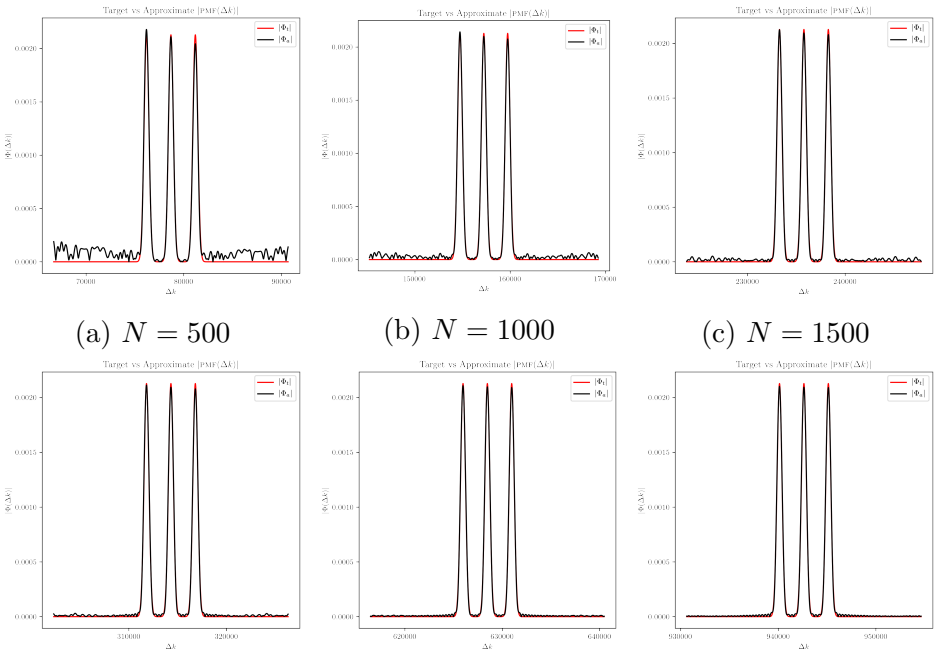

(a) $N = 500$ (b) $N = 1000$ (c) $N = 1500$

(d) $N = 2000$ (e) $N = 4000$ (f) $N = 6000$

Figure 6.4: Comparing the approximate vs target PMF while varying the number of domains and keeping the length fixed.

In Fig. 6.4 we find that as we increase the number of domains the approximate PMF gets closer to the target. The approximate PMF becomes more accurate because as we increase N, we are increasing the resolution of the tracking amplitude. We show this effect in greater detail in Fig. 6.5, where we plot the target and approximate amplitude for a target PMF that has five Gaussian peaks and vary the number of domains over $N = 1000, 6000$. In the top two plots of Fig. 6.5, we see that by increasing N we can increase the resolution of the tracking amplitude (black) which can better approximate the target. In the bottom two plots of Fig. 6.5 we see the difference that it makes when approximating the target PMF.

Comparing Fig. 6.4 and 6.5 we find that the optimal value of N is when each domain length is smaller then the period of oscillation of the target PMF.

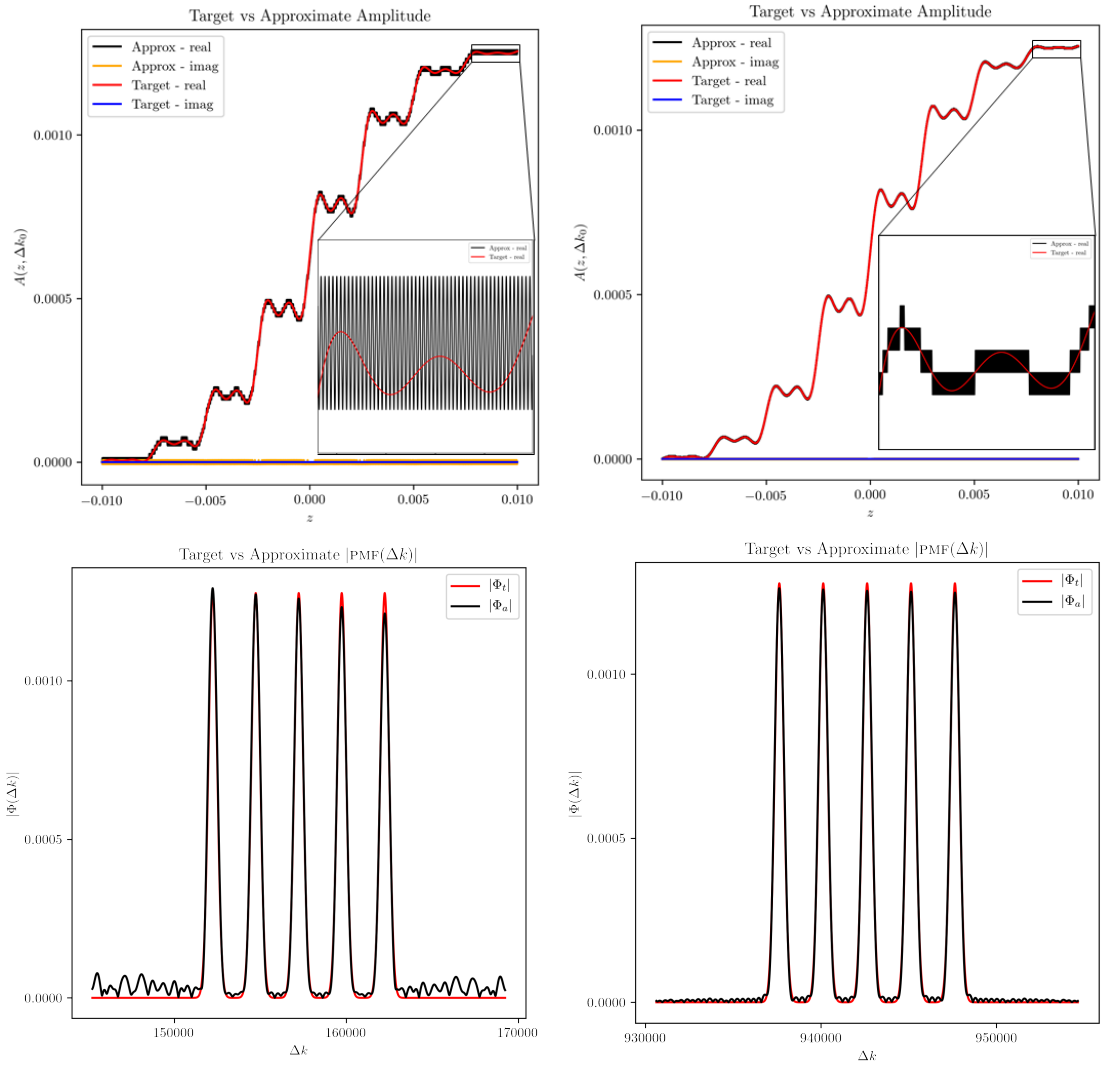

(a) $N = 1000$

(b) $N = 6000$

Figure 6.5: Comparing the PMF and amplitude for $N = 1000$ and $N = 6000$.

6.2 Fabrication Errors

In Section 2.4.4 we described that given a crystal, we can change the nonlinearity of a section by ferroelectrically poling it. We change the nonliearity by applying an electrode that applies an electric field which slowly changes the polarization to point in the oppo-

site direction. In Section 2.5.2, we detailed an algorithm that, given a target PMF, will produce the nonlinearity profile which generates the associated PMF that approximates the target PMF. Putting these two parts together we are able to design and engineer a crystal that will generate a PMF with desired properties, however, it is inevitable that there will be imperfections during the fabrication process. In this section, we discuss the possible imperfections that may arise during the engineering process and simulate them to determine there effect on the final PMF.

For realistic scenarios, there are three main possible sources of error [55] shown schematically in Fig. 6.6 and given by

1. Overpoling and underpoling regions: The size of the domain generated depends on the length of time the electrode is on and in contact with the crystal. Uncertainties in the time can then lead to imperfections in domain sizes.

2. Randomized variations in wall positions: Since we are dealing with crystals on the order of mm and electrodes on the order of μm there is a possibility that the electrode itself was placed in the wrong location thus leading to slightly randomized domain positions.

3. Missed domains when poling: This source of error can occur if some sets of electrodes are faulty leading to a region not being flipped at all or since the domain sizes are so small (on the order of μm) it is possible for some adjacent domains to bond together. These both lead to a situation where a domain was wrongly poled/unpoled.

It was shown by Kelly-Massicotte in [55], that for periodic poling, imperfections due to overpoling or underpoling did not have a large effect on the amplitude and purity of the PMF. However, in [55] it was shown that for periodic poling, variations in domain wall positions and missed domains had a large effect on the generated amplitude and lead to a significant decrease as the errors were increased. With this in mind, we will focus on implementing a randomized error to mimic missed domains.

We begin by running the algorithm to produce the nonlinearity profile for a PMF with three Gaussian peaks. Once we generate the nonlinearity profile we will simulate error randomly. We assign p to be the probability that a given domain is not missed and the value $1 - p$, the probability that a domain was missed and set the nonlineairty in that domain to be $+1$. We then iterate through for every domain.

We compare the results by plotting the nonlinearity profile, amplitude and PMF. Choosing a success rate of $p = 95\%$ we ran the process five times to get a better picture of the

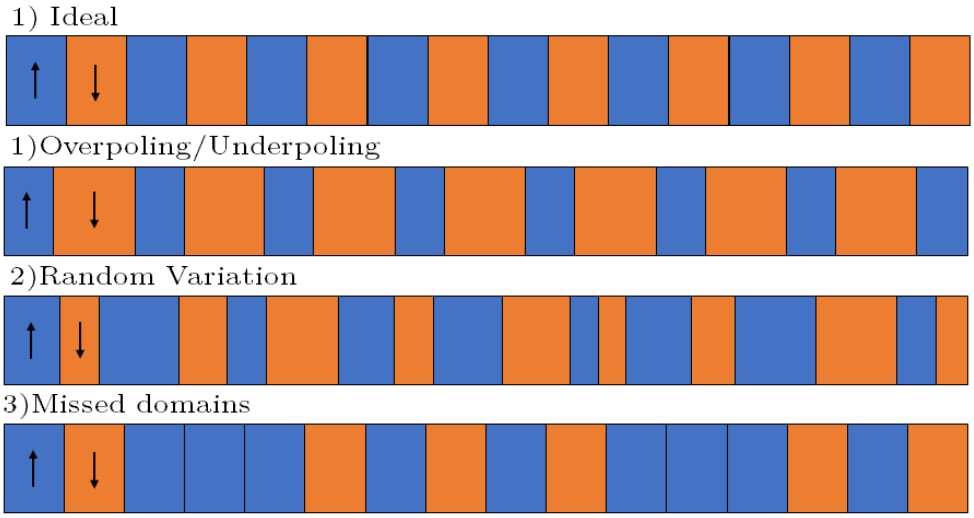

Figure 6.6: Schematic of the main sources of error when ferroelectrically poling a crystal.

randomized result. In Fig. 6.7 we plot the actual nonlinearity profile and under it, five randomized errors. In Fig. 6.8 we compare the target amplitude, the approximate amplitude and five trials of the randomized nonlinearity. Finally, in Fig. 6.9 we plot the target PMF, approximate PMF and the PMF from the five randomized nonlinearity profiles. The randomized error in the nonlinearity profile leads to a decrease of amplitude and an increase in noise. The decreased amplitude is not a large error because we can always increase the amplitude of the pump function. However, the more noise the PMF has the less accurate the decomposition we provided in Chapter 3 is.

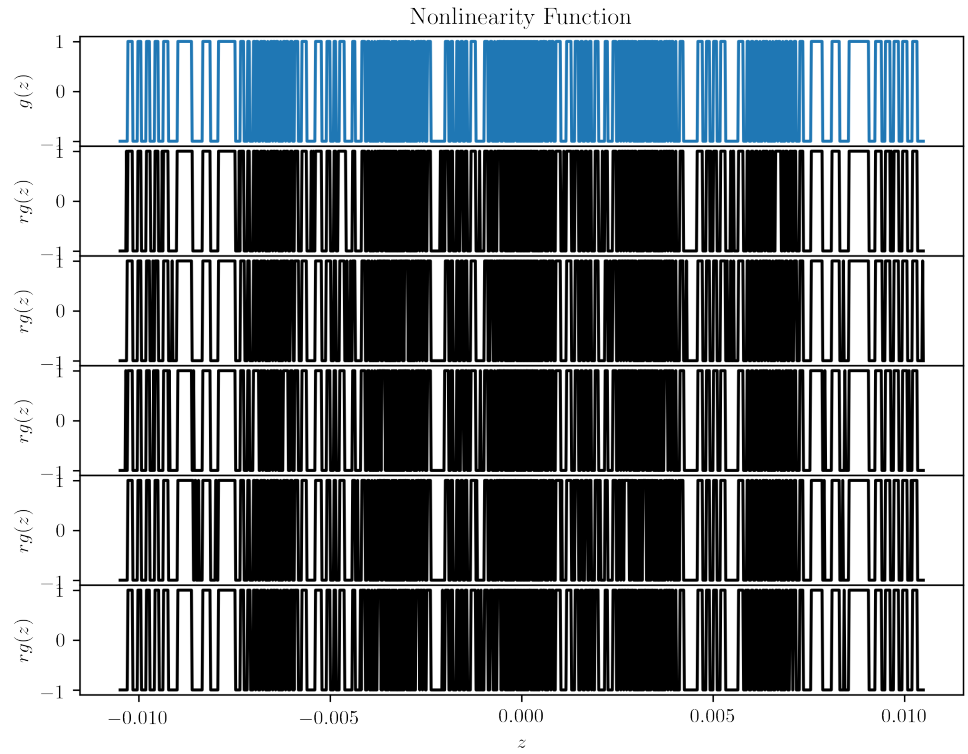

Figure 6.7: Comparing the approximate nonlinearity (top) to five sets of randomized errors.

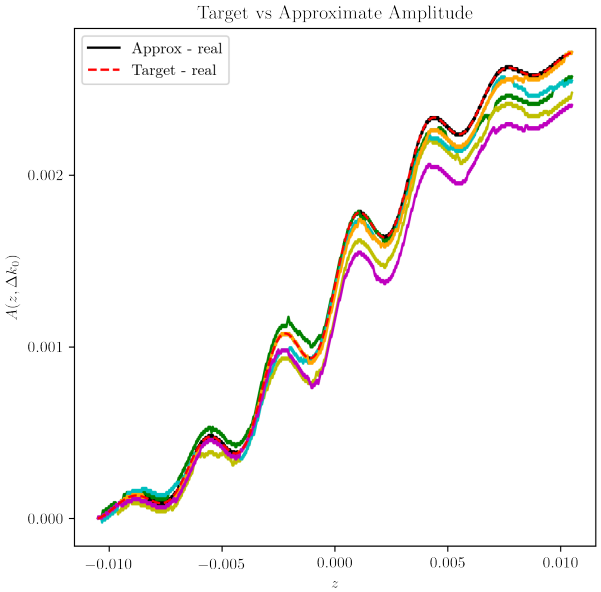

Figure 6.8: Comparing the target amplitude, the approximate amplitude and five trials of the random error nonlinearity

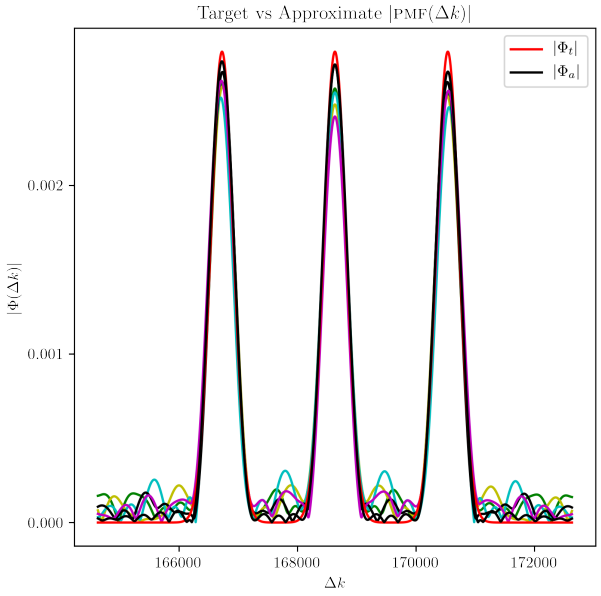

Figure 6.9: Comparing the target PMF, approximate PMF and the PMF from the five random error nonlinearity profiles.

Chapter 7

Conclusion

In this thesis we proposed a method for generating two non-standard Gaussian states of quantum light. The first state we defined is a "tuneable hybrid squeezed state", which contains the properties of both single- and two-mode squeezed states. The second are multimode squeezed states. Our states are encoded in Gaussian frequency modes, and our method relies on customizing the joint spectral properties of light via a quantum nonlinear-optical process called spontaneous parametric down conversion. Customizing the joint spectral properties of the generated light requires two independent ingredients. The first is the spectral engineering of the light incident inside the crystal. The second is the engineering of the nonlinear crystal to have desired phasematching properties (captured by something known as the "phasematching function").

The phasematching function is related to the nonlinearity throughout the crystal via the Fourier transform. To shape the phasematching function to have desired properties, we need to engineer the nonlinearity of the crystal. While in theory, the nonlinearity is a continuous function, for practical solid crystals, it varies between ± 1. To design nonlinear crystals we use the deterministic algorithm proposed in [44], which takes as an input, the target phasematching function, and outputs a string of $+1$'s and -1's, which is the desired nonlinearity profile. The nonlinearity profile is then engineered into the crystal by Ferroelectrically poling the material [38].

We analysed the limitations of the possible phasematching functions that can be generated via engineering a nonlinear crystal. We found that the phasematching function must be symmetric, the amplitude coefficients of each Gaussian must satisfy an upper bound, and determined that for a given crystal with length L, the number of Gaussians is not dependent on L and the optimal width of each Gaussian is $\sigma = 5/L$.

Next we examined some sources of error when designing a phasematching function with desired properties. We found that if the amplitude of the phasematching function has oscillations with a period on the same order of magnitude as the domain length, we cannot generate the phasematching function because we cannot accurately approximate the amplitude. We proposed that to mitigate this error we should always choose the amplitude coefficients to satisfy their upper bound and showed that one can achieve a finer resolution by increasing the number of domains, which is equivalent to decreasing the domain length.

Lastly, we examined possible errors associated with the fabrication of a crystal. We introduced fabrication errors into the nonlinear material by simulating missed domains and determined that the error does not have an affect on the amplitude of the phasematching function but introduces noise. The noise introduced leads to errors in the decomposition of the joint spectral amplitude by Gaussian functions.

Our method puts the modes of the electromagnetic field into Gaussian frequency distributions which provides three advantages over the previous approach in [16, 17, 18, 15]. The first advantage is that the states we generate are localized in time-frequency, allowing for high dimensional encoding that are compatible with waveguides and fiber transmission [19]. The second advantage is unlike the localized time-frequency modes of the Schmidt decomposition, [19] which are hard to experimentally distinguish [20], our modes are defined by Gaussian distributions at center frequencies, making them easy to experimentally distinguish. Lastly, the states generated by [15, 16] which used beam splitters to generate entangled states in the spatial modes of the field, whereas ours are in the same spatial mode which makes the experiment more stable. Our method is tunable, scaleable to many modes and the entangled states are all simultaneously available.

As a future project we would like to see a crystal designed to generate these multimode squeezed states and verify them experimentally. One can also begin analyzing these states for other areas of research, such as, the field of microscopy [56] and the fabrication of microscale medical devices [57], which both use squeezed states to their advantage.

Quantum states of light can be transferred over long distances without degrading and posses all the interesting quantum properties that we desire, such as, superposition and entanglement. These properties make quantum states of light ideal for a variety of quantum information protocols [58, 8, 3, 4]. Hybrid squeezed states have the advantage that they have both properties of single- and two-mode squeezed states. Hybrid squeezed states have more parameters that we can control, which makes them useful for approximating non-Gaussian states via post-selection. We speculate that hybrid squeezed states would lead to more accurate results for multi-parameter quantum metrology, since they combine the noise-reducing properties of single-mode squeezed states with the entanglement of

two-mode squeezed states. By providing a source for multimode squeezed states, where the modes are localized in time-frequency, we allow the generalization of many quantum information protocols to their multimode counterparts, such as, multi-parameter quantum metrology [12], multi-channel quantum imaging [13] and multi-partite teleportation [14].

References

[1] Gregory David Miller. *Periodically poled lithium niobate: modeling, fabrication, and nonlinear-optical performance*. PhD thesis, Stanford university, 1998.

[2] Agata M Brańczyk, Alessandro Fedrizzi, Thomas M Stace, Tim C Ralph, and Andrew G White. Engineered optical nonlinearity for quantum light sources. *Optics express*, 19(1):55–65, 2011.

[3] GJ Milburn and Samuel L Braunstein. Quantum teleportation with squeezed vacuum states. *Physical Review A*, 60(2):937, 1999.

[4] Mark Hillery. Quantum cryptography with squeezed states. *Physical Review A*, 61(2):022309, 2000.

[5] Ramil Nigmatullin, Christopher J Ballance, Niel De Beaudrap, and Simon C Benjamin. Minimally complex ion traps as modules for quantum communication and computing. *New Journal of Physics*, 18(10):103028, 2016.

[6] Seth Lloyd and Samuel L Braunstein. Quantum computation over continuous variables. In *Quantum information with continuous variables*, pages 9–17. Springer, 1999.

[7] Ryan S Bennink, Sean J Bentley, Robert W Boyd, and John C Howell. Quantum and classical coincidence imaging. *Physical review letters*, 92(3):033601, 2004.

[8] Roman Schnabel, Nergis Mavalvala, David E McClelland, and Ping K Lam. Quantum metrology for gravitational wave astronomy. *Nature communications*, 1(1):1–10, 2010.

[9] Xiang-Bin Wang, Tohya Hiroshima, Akihisa Tomita, and Masahito Hayashi. Quantum information with gaussian states. *Physics reports*, 448(1-4):1–111, 2007.

[10] Christian Weedbrook, Stefano Pirandola, Raúl García-Patrón, Nicolas J Cerf, Timothy C Ralph, Jeffrey H Shapiro, and Seth Lloyd. Gaussian quantum information. *Reviews of Modern Physics*, 84(2):621, 2012.

[11] A. I. Lvovsky. Squeezed light, 2014.

[12] Manuel Gessner, Luca Pezzè, and Augusto Smerzi. Sensitivity bounds for multiparameter quantum metrology. *Physical review letters*, 121(13):130503, 2018.

[13] Ivan V Sokolov and Mikhail I Kolobov. Squeezed-light source for superresolving microscopy. *Optics letters*, 29(7):703–705, 2004.

[14] Yimin Lian, Changde Xie, and Kunchi Peng. Continuous variable multipartite entanglement and optical implementations of quantum communication networks. *New Journal of Physics*, 9(9):314, 2007.

[15] Guy Yeoman and Stephen Mark Barnett. Two-mode squeezed gaussons. 1993.

[16] Peter van Loock and Samuel L Braunstein. Multipartite entanglement for continuous variables: a quantum teleportation network. *Physical Review Letters*, 84(15):3482, 2000.

[17] Olivier Pfister, Sheng Feng, Gregory Jennings, Raphael Pooser, and Daruo Xie. Multipartite continuous-variable entanglement from concurrent nonlinearities. *Physical Review A*, 70(2):020302, 2004.

[18] Nicolas C Menicucci, Steven T Flammia, Hussain Zaidi, and Olivier Pfister. Ultracompact generation of continuous-variable cluster states. *Physical Review A*, 76(1):010302, 2007.

[19] Vahid Ansari, John M Donohue, Benjamin Brecht, and Christine Silberhorn. Tailoring nonlinear processes for quantum optics with pulsed temporal-mode encodings. *Optica*, 5(5):534–550, 2018.

[20] Andreas Eckstein, Benjamin Brecht, and Christine Silberhorn. A quantum pulse gate based on spectrally engineered sum frequency generation. *Optics express*, 19(15):13770–13778, 2011.

[21] Quesada Mejia and Juan Carlos Martín Nicolás. *Very Nonlinear Quantum Optics*. PhD thesis, University of Toronto, 2015.

[22] Navin AR Bhat and JE Sipe. Hamiltonian treatment of the electromagnetic field in dispersive and absorptive structured media. *Physical Review A*, 73(6):063808, 2006.

[23] Marlan O. Scully and M. Suhail Zubairy. *Quantum Optics*. Cambridge University Press, 1997.

[24] K Priyashanka and K.A.I.L. GAMALATH. Coherent states in a laser cavity. *International Letters of Chemistry, Physics and Astronomy*, 56:71–86, 07 2015.

[25] Timothy C Ralph, Alexei Gilchrist, Gerard J Milburn, William J Munro, and Scott Glancy. Quantum computation with optical coherent states. *Physical Review A*, 68(4):042319, 2003.

[26] Gan Qin, Ke-lin Wang, and Tong-zhong Li. General multimode squeezed states. *arXiv preprint quant-ph/0109020*, 2001.

[27] Lev Vaidman. Teleportation of quantum states. *Physical Review A*, 49(2):1473, 1994.

[28] Masahiro Takeoka, Masahide Sasaki, and Masashi Ban. Continuous variable teleportation as a quantum channel. *Optics and Spectroscopy*, 94(5):675–683, 2003.

[29] P Van Loock, Samuel L Braunstein, and HJ Kimble. Broadband teleportation. *Physical Review A*, 62(2):022309, 2000.

[30] Ulf Leonhardt. Quantum physics of simple optical instruments. *Reports on Progress in Physics*, 66(7):1207, 2003.

[31] Alicia Sit, Lambert Giner, Ebrahim Karimi, and Jeff S Lundeen. General lossless spatial polarization transformations. *Journal of Optics*, 19(9):094003, 2017.

[32] Ramamurti Shankar. *Principles of quantum mechanics*. Springer Science & Business Media, 2012.

[33] Nicolás Quesada and JE Sipe. Why you should not use the electric field to quantize in nonlinear optics. *Optics letters*, 42(17):3443–3446, 2017.

[34] CK Law, Ian A Walmsley, and JH Eberly. Continuous frequency entanglement: effective finite hilbert space and entropy control. *Physical Review Letters*, 84(23):5304, 2000.

[35] Robert W Boyd. *Nonlinear optics*. Academic press, 2019.

[36] Gorachand Ghosh. Sellmeier coefficients and dispersion of thermo-optic coefficients for some optical glasses. *Applied optics*, 36:1540–6, 04 1997.

[37] Q Chen and WP Risk. Periodic poling of ktiopo/sub 4/using an applied electric field. *Electronics Letters*, 30(18):1516–1517, 1994.

[38] M Yamada, N Nada, M Saitoh, and K Watanabe. First-order quasi-phase matched linbo3 waveguide periodically poled by applying an external field for efficient blue second-harmonic generation. *Applied Physics Letters*, 62(5):435–436, 1993.

[39] W Kanzig. Solid state physics, vol. 4. *Seitz and D. Turnbull, Eds. New York: Academic*, pages 1–197, 1957.

[40] Agata M Brańczyk, TC Ralph, Wolfram Helwig, and Christine Silberhorn. Optimized generation of heralded fock states using parametric down-conversion. *New Journal of Physics*, 12(6):063001, 2010.

[41] P. Ben Dixon, Jeffrey H. Shapiro, and Franco N. C. Wong. Spectral engineering by gaussian phase-matching for quantum photonics. *Opt. Express*, 21(5):5879–5890, Mar 2013.

[42] Annamaria Dosseva, Łukasz Cincio, and Agata M Brańczyk. Shaping the joint spectrum of down-converted photons through optimized custom poling. *Physical Review A*, 93(1):013801, 2016.

[43] JL Tambasco, A Boes, LG Helt, MJ Steel, and A Mitchell. Domain engineering algorithm for practical and effective photon sources. *Optics express*, 24(17):19616–19626, 2016.

[44] Francesco Graffitti, Dmytro Kundys, Derryck T Reid, Agata M Brańczyk, and Alessandro Fedrizzi. Pure down-conversion photons through sub-coherence-length domain engineering. *Quantum Science and Technology*, 2(3):035001, 2017.

[45] Ivan Marcikic, Hugues De Riedmatten, Wolfgang Tittel, Hugo Zbinden, Matthieu Legré, and Nicolas Gisin. Distribution of time-bin entangled qubits over 50 km of optical fiber. *Physical Review Letters*, 93(18):180502, 2004.

[46] Michael Kues, Christian Reimer, Piotr Roztocki, Luis Romero Cortés, Stefania Sciara, Benjamin Wetzel, Yanbing Zhang, Alfonso Cino, Sai T Chu, Brent E Little, et al. On-chip generation of high-dimensional entangled quantum states and their coherent control. *Nature*, 546(7660):622–626, 2017.

[47] Andreas Christ, Cosmo Lupo, and Christine Silberhorn. Exponentially enhanced quantum communication rate by multiplexing continuous-variable teleportation. *New Journal of Physics*, 14(8):083007, 2012.

[48] Benjamin Brecht, Andreas Eckstein, Raimund Ricken, Viktor Quiring, Hubertus Suche, Linda Sansoni, and Christine Silberhorn. Demonstration of coherent time-frequency schmidt mode selection using dispersion-engineered frequency conversion. *Physical Review A*, 90(3):030302, 2014.

[49] LG Helt, Agata M Brańczyk, Marco Liscidini, and MJ Steel. Parasitic photon-pair suppression via photonic stop-band engineering. *Physical Review Letters*, 118(7):073603, 2017.

[50] Andrew M Weiner. Ultrafast optical pulse shaping: A tutorial review. *Optics Communications*, 284(15):3669–3692, 2011.

[51] Seiji Armstrong, Jean-François Morizur, Jiri Janousek, Boris Hage, Nicolas Treps, Ping Koy Lam, and Hans-A Bachor. Programmable multimode quantum networks. *Nature communications*, 3(1):1–8, 2012.

[52] Michael Epping, Hermann Kampermann, Dagmar Bruß, et al. Multi-partite entanglement can speed up quantum key distribution in networks. *New Journal of Physics*, 19(9):093012, 2017.

[53] AI Lvovsky, Philippe Grangier, Alexei Ourjoumtsev, Valentina Parigi, Masahide Sasaki, and Rosa Tualle-Brouri. Production and applications of non-gaussian quantum states of light. *arXiv preprint arXiv:2006.16985*, 2020.

[54] MS Elezov, ML Scherbatenko, DV Sych, and GN Goltsman. Active and passive phase stabilization for the all-fiber michelson interferometer. In *Journal of Physics: Conference Series*, volume 1124, 2018.

[55] Jérémy Kelly-Massicotte. Customized nonlinearity shaping in imperfect or variable waveguides. Master's thesis, University of Waterloo, 2019.

[56] Winfried Denk, James H Strickler, and Watt W Webb. Two-photon laser scanning fluorescence microscopy. *Science*, 248(4951):73–76, 1990.

[57] Shaun D Gittard, Alexander Nguyen, Kotaro Obata, Anastasia Koroleva, Roger J Narayan, and Boris N Chichkov. Fabrication of microscale medical devices by two-photon polymerization with multiple foci via a spatial light modulator. *Biomedical optics express*, 2(11):3167–3178, 2011.

[58] Samuel L Braunstein and Peter Van Loock. Quantum information with continuous variables. *Reviews of modern physics*, 77(2):513, 2005.

[59] Ulrik L Andersen, Tobias Gehring, Christoph Marquardt, and Gerd Leuchs. 30 years of squeezed light generation. *Physica Scripta*, 91(5):053001, 2016.

[60] Properties of KTP/KTA Single Crystal. https://www.unitedcrystals.com/KTPProp.html, 2020. [Online; accessed 18-July-2020].

[61] CF Lo and R Sollie. Correlated-squeezed-state approach for phonon coupling in a tunneling system. *Physical Review B*, 44(10):5013, 1991.

APPENDICES

Appendix A

Phase Matching Function Constraints

In section 2.5.2 we introduced two constraints, that the target PMF could not have a slope larger than $2/\pi$. To demonstrate this restriction we take the target PMF to be a Gaussian centered at Δk_0 with a constant multiplier a and calculate the slope of the amplitude to be

$$\frac{dA_t(\Delta k_0, z)}{dz} = \frac{a_0}{2\pi} e^{-z^2\sigma^2/2} \leq \frac{2}{\pi}, \quad \forall z. \tag{A.1}$$

The slope of the target amplitude is at its maximum when $z = 0$, so we conclude that $a_0 \leq 4$. In Fig. A.1 we compare a Gaussian target PMF with two different pre-factors, one with a max value of $a_0 = 4$ and the other larger with $a_0 = 5$. We find that when the PMF has the correct pre-factor we can track the target amplitude. However, when we increase the pre-factor above the max we see a deviation from the target to approximate amplitude.

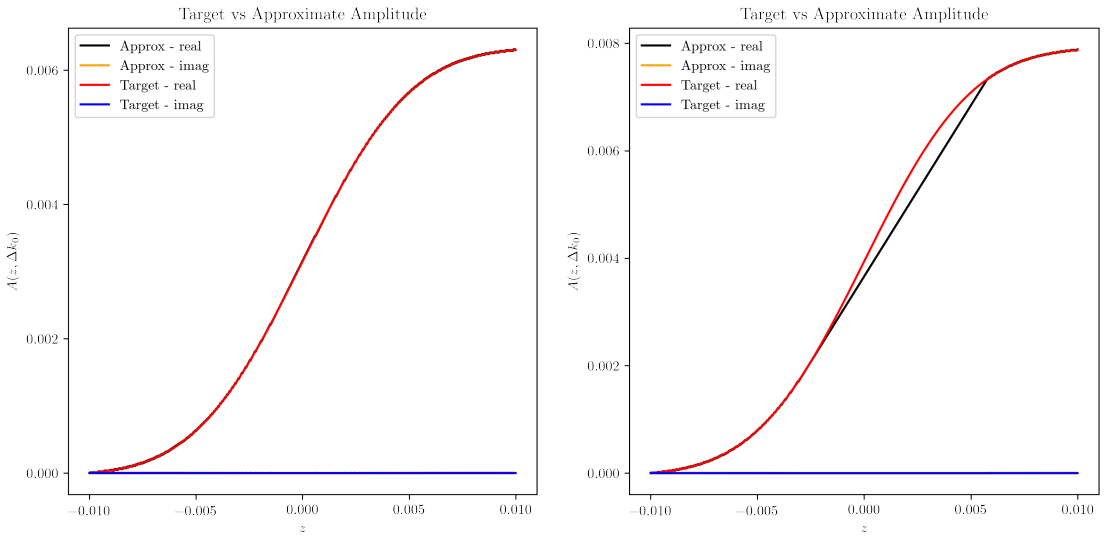

(a) Pre-factor of $a_0 = 4$.

(b) Pre-factor of $a_0 = 5$.

Figure A.1: Plotting the amplitude throughout the crystal of a Gaussian target PMF with two different pre-factors. We can see that when we exceed the restriction of the slope of the target amplitude of $2/\pi$ we can no longer approximate the target.

Appendix B

Example of Custom Phase Matching Function

In this section we provide all of the physical parameters used in this thesis to design nonlinear crystals and provide a complete example of tailoring a nonlinear crystal to have a desired PMF

Throughout this thesis we use a Type II Potassium titanyl phosphate crystal pumped by a center frequency $\Omega_p = 2.53 \times 10^{15}\text{s}^{-1}$ [$\lambda_p = 6.75 \times 10^{-8}\text{m}$] which generates signal and idler photons at center frequencies $\Omega_s = 1.26583 \times 10^{15}\text{s}^{-1}$ [$\lambda_s = 1.37 \times 10^{-7}\text{m}$] and $\Omega_i = 1.26583 \times 10^{15}\text{s}^{-1}$ [$\lambda_i = 1.30 \times 10^{-7}\text{m}$]. The signal and idler photons have orthogonal polarization and the signal photons have the same polarization as the pump. The Sellmier parameters for the KTP crystal are given by $(A_1, A_2, A_3, A_4) = (3.0065, 0.03901, 0.04547, 0.01408)$ and $(B_1, B_2, B_3, B_4) = (3.3134, 0.05694, 0.05658, 0.01692)$ where the A's correspond to the pump and signal polarization and the B's to the idler [60]. The crystal is group velocity matched such that the PMF is always on the diagonal. The phase mismatch evaluated at zeroth order for the center signal and idler frequencies is given by $\Delta k_0 = 169000\text{m}^{-1}$. We chose the length of the crystal to be typical and given by $L = 2.0\text{cm}$.

B.1 Gaussian PMF

We now choose a target PMF and use the algorithm described in section 2.5.2 to determine the nonlinearity profile and calculate the PMF. In this example, the target PMF will be a

Gaussian given by

$$\Phi_t(\Delta k) = a_0 e^{-\frac{(\Delta k - \Delta k_0)^2}{2\sigma^2}}, \tag{B.1}$$

which is centered at Δk_0. We take the amplitude coefficient to be the max at $a_0 = 4$ from the discussion in section 6.1.2 and the width to be $\sigma = 5/L$ per the discussion in section 6.1.3.

The algorithm takes the target PMF and calculates the nonlinearity in Fig. B.1. We then calculate the target amplitude from the target PMF and compare it with the approximate amplitude due to the nonlinearity profile in Fig. B.1. In Fig. B.2 we plot the target and approximate field amplitude. Lastly, we calculate the approximate PMF using Eq. (2.54) and compare it to the target PMF in Fig. B.3, the two plots are in good agreement.

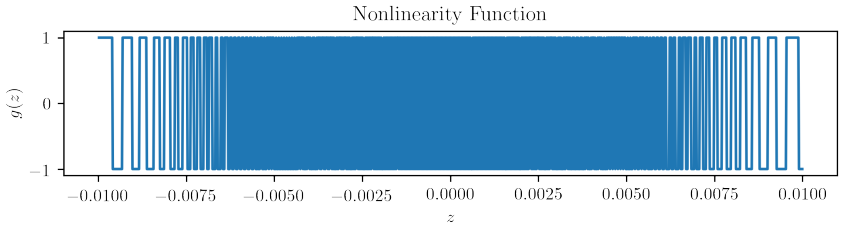

Figure B.1: Non linearity profile for a target Gaussian PMF.

We then choose the pump function to be a Gaussian with the same width. Multiplying these two functions together gives the JS.In Fig. B.4 we plot the PMF,pump and JSA.

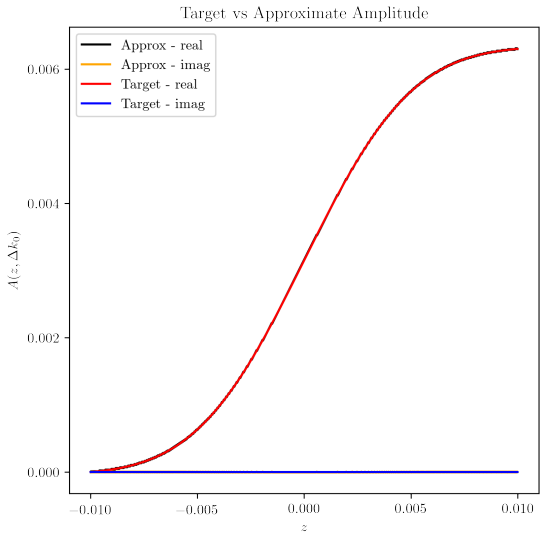

Figure B.2: Comparing the target amplitude to the approximate amplitude for a Gaussian target PMF

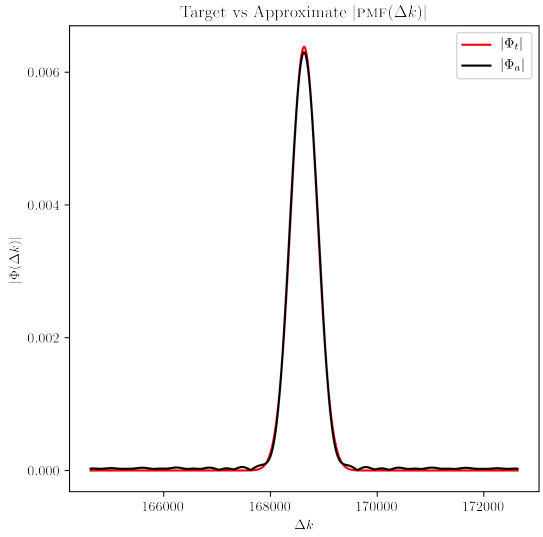

Figure B.3: Gaussian centered at Δk_0 compared to engineered PMF

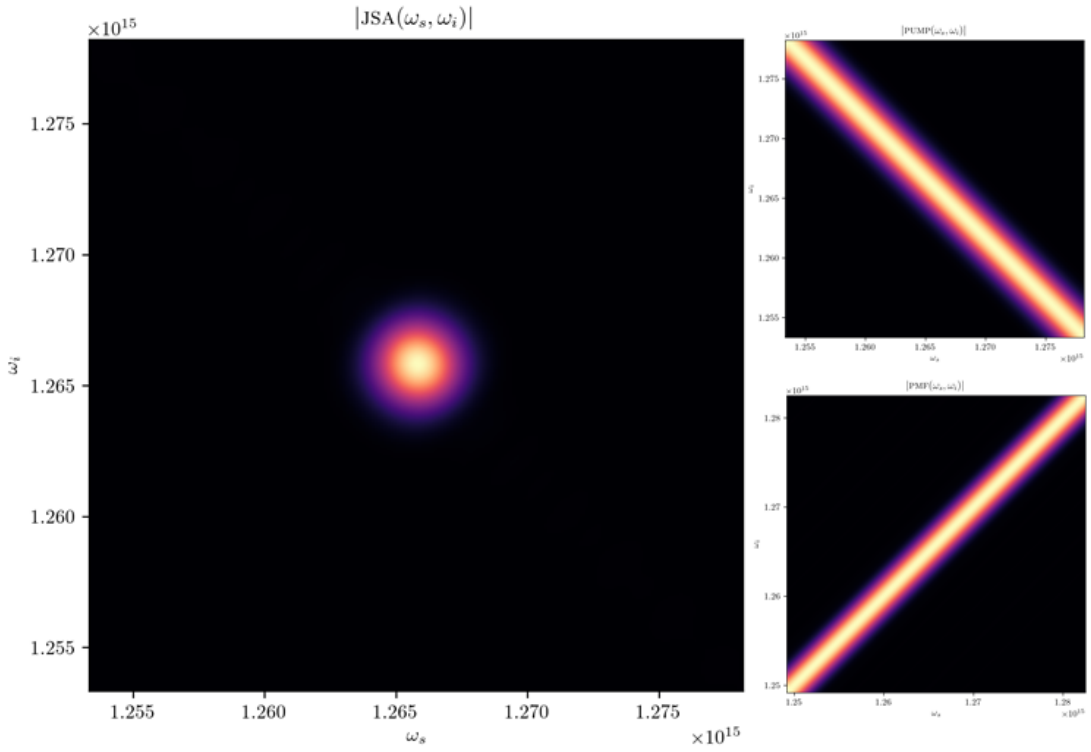

Figure B.4: Plotting the JSA, PMF (lower plot) and pump (upper plot).